Master's Thesis

Carbonization Study of Cellulose Nanocrystals and Super Engineering Plastic Based Nano Composite Fibers

SungMin Son

Department of Materials Science and Engineering

Graduate School of UNIST

2018

Carbonization Study of Cellulose Nanocrystals and Super Engineering Plastic Based Nano Composite Fibers

SungMin Son

Department of Materials Science and Engineering

Graduate School of UNIST

Carbonization Study of Cellulose Nanocrystals and Super Engineering Plastic Based Nano Composite Fibers

A thesis/dissertation
submitted to the Graduate School of UNIST
in partial fulfillment of the
requirements for the degree of
Master of Science

SungMin Son

5. 29. 2018 of submission
Approved by

Advisor
Han Gi Chae

Carbonization Study of Cellulose Nanocrystals and Super Engineering Plastic Based Nano Composite Fibers

SungMin Son

This certifies that the thesis/dissertation of SungMin Son is approved.

5. 29. 2018 of submission

Advisor: Han Gi Chae

Myoung Hoon Song

Hyun-Wook Lee

Abstract

Cellulose Nanocrystals (CNC) have been regarded as a versatile precursor for carbon nanomaterials. CNC can be converted into carbon materials by hydrothermal treatment and subsequent carbonization process. Due to high crystallinity and structural regularity of CNC, carbonized CNC would give well-ordered graphitic structure compared to other cellulose-based carbon materials. In chapter 2, carbonization study of CNC covers the effect of heat treatment conditions on the structural development mechanism of CNC over the range of carbonization temperature from 1000 to 2500 °C. We have conducted experiments to study the effect of oxidative stabilization process on the structural development of CNC-based graphite. Compared to the carbonization mechanism of pristine CNC, stabilized CNC was prepared by heat treatment at 250 °C for 1hr. In addition, the resultant graphitic structure of carbonized cellulose nanocrystals was systemically analyzed by transmission electron microscopy, x-ray photoelectron spectroscopy, and Raman spectroscopy. TEM data clarified that carbonized CNC prepared from stabilized samples (S-cCNC) gave rise to more highly ordered graphitic structure with little distortion site and defect points compare to D-cCNC over the whole temperature range of carbonization. Structural development mechanisms of both C- and S-cCNCs were systematically traced by Raman spectroscopy. Peak fitting results of Raman spectra evidenced structural conversion from disordered carbon to the graphitic structure.

In chapter 3, PES/CNC composite fibers were prepared by dry-jet wet spinning and their morphology and tensile properties were characterized. CNC with high Young's modulus, crystallinity and aspect ratio can be regarded as a nano-size reinforcing agent. Dispersion of CNC was investigated by Dynamic Light Scattering (DLS) and Scanning Electron Microscopy (SEM). Upon using bath-type sonication with a power of 20 J/s, 48 hr sonication time was required to obtain well-dispersed CNC phase in *N*,*N*-Dimethylacetamide (DMAc). Experimental results showed that the tensile modulus of PES/CNC1 composite fibers were 4.7 GPa about 17% higher than control PES fibers.

Table of Content

List of Tables

List of Figures

Chapter I. Introduction to cellulose nanocrystals

1.1 Cellulose Nanocrystals (CNC)

Cellulose is the most abundant renewable organic materials produced in the biosphere. Cellulose is distributed in higher plants, marine animals, algae, fungi, bacteria, invertebrates, etc. Cellulose can be thought as a high molecular weight homopolymer of β-1,4-anhydro-D-glucose units [1, 2]. The number of glucose units is up to 20000 [2, 3]. Unlike other inorganic materials like carbon nanotube and Vapor-grown carbon nanofibers, cellulose nanocrystals are not chemically synthesized from molecular or atomic components. Cellulose chains are aggregated in microfibrils through van der waals force and both intra and inter molecular hydrogen bonding. They are extracted many resources from bacterial, wood pulp, cotton, and sea animals. Also, the plants and the primary carbon resources on Earth which can convert carbon dioxide to biomass through photosynthesis. These precursors are typical biomass composites, which are mainly composed of cellulose, hemicellulose, and lignin. In the cell wall, it is composed of approximately 36 individual cellulose molecule chains assemble due to through hydrogen bonds between the chains and form elementary fibrils, which are further packed into larger microfibrils. However, cellulose from different resources may occur in different packing ways by the biosynthesis conditions. Due to high crystallinity and high orientation of cellulose nanocrystals, it exhibits theoretical Young's modulus of 206 GPa along [001] planes and a tensile strength of nearly 10 GPa. The dimensions of cellulose nanocrystals that obtained from acid hydrolysis have 5-10 nm in width and approximately 200 nm in length.

Individual cellulose molecules are assembled into elementary fibrils, which pack into larger units called microfibrils, and these again assembled into cellulose fibers. Cellulose chains are aggregated in microfibrils through van der Waals force and both intra- and inter-molecular hydrogen bonding. Cellulose I, II, III_I, IV_I and IV_{II} have been identified due to different hydrogen bonding network and molecular orientation in cellulose. Cellulose I have two suballomorphs I_α which is usually celluloses from algae and bacteria, and I_β which is common in cellulose from cotton, wood, and ramie. They differ in their hydrogen bonding patterns. As a result, I_α corresponds to a one-chain triclinic P1 unit cell, whereas I_β exist in two chains monoclinic $P2_1$ unit cell. Cellulose II can be obtained by chemical regeneration or mercerization with changing in the hydrogen bond network. Cellulose II exists in a monoclinic $P2_1$ unit cell [4].

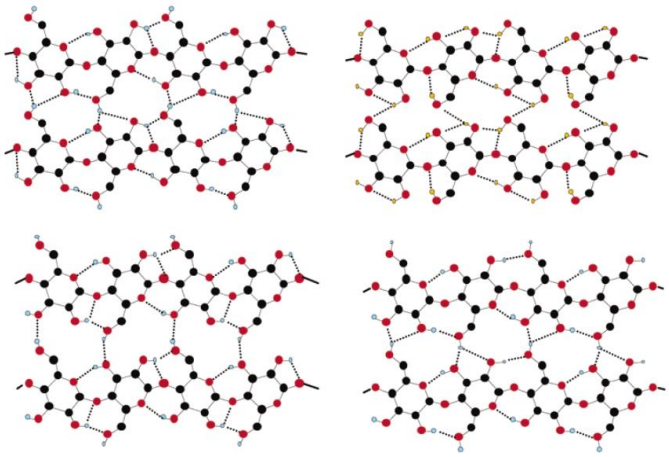

Figure 1.1. Hydrogen-bonding patterns in cellulose $\mathbf{I}_{\alpha}$ and $\mathbf{I}_{\beta}$ based on the crystal structures of Nishyama et al. Top left and right: the two alternatives hydrogen-bond networks in cellulose $\mathbf{I}_{\alpha}$. Bottom: the dominant hydrogen-bond network in cellulose $\mathbf{I}_{\beta}$: (left) chains at the origin of the unit cell; (right) chains at the center of the unit cell [5].

Depending on dimension, functions, and preparation of methods, nanocellulose fiber can be divided into three types. Firstly, Micro fibrillated cellulose (MFC) is derived by treating microscale cellulose fibers using a variety of techniques including chemical treatment and mechanical homogenization. MFC is referred to as “microcrystalline cellulose”, “microcrystallite”, “cellulose nanofibrils” and “microfibrils”. The second type of cellulose is referred to as nanocrystalline cellulose (NC) or nanowhiskers also called “nanocellulose whiskers”, “nanocrystals”, “monocrystals”, “cellulose rod-like nanocrystals” and whiskers. NC is composed of the crystalline regions present in MFC, with the regions being liberated by the mechanical, ultrasonic and chemical process to remove the amorphous regions. The final type of cellulose is called as bacterial nanocellulose which also appears in the literature as “bacterial cellulose” which also appears in the literature as “bacterial cellulose”, “microbial cellulose” and “biocellulose” [6-9].

1.2 Preparation of Cellulose Nanocrystals

Microcrystalline celluloses (MCCs) are purified and depolymerized cellulose particles. Cellulose nanocrystals are obtained by mechanical size reduction and acid hydrolysis from plants. Mechanical size reduction such as high pressure homogenizer and cryocrushing were used to be obtain the MCCs. And then CNC can be obtained by acid hydrolysis of cellulose microfibrils. Since amorphous arts are vulnerable to acid, acid treatment leaves only the crystalline part, which is cellulose nanocrystals. CNC are rod-like or whisker-shaped particles with a diameter in the range of 3-20 nm and length in the range

of 100-600 nm, which are different depending on the source of cellulose [3]. CNC can be obtained through acid hydrolysis of MCCs, microfibrillated celluloses (MFCs), or nanofibrillated celluloses (NFCs) [1].

Isolation of cellulose nanoparticles has been performed by acid hydrolysis and mechanical treatment [4]. Strong mechanical treatment leads to the extraction of microfibrils with high aspect ratio. The obtained products called MFCs. CNC is prepared by hydrolysis with hydrochloric acid, phosphoric acid, and sulfuric acid.

1.2.1 Mechanical size reduction

Mechanical processes were used to isolate cellulose nanofibers produce high shear that causes transverse cleavage along the longitudinal axis of the cellulose microfibrillar structure, resulting in the extraction of long cellulose microfibrils [10]. High-pressure homogenizer with cavitation, shear, and impact forces had broken down the cell walls of the microfibers and obtained the desired nanofibrils. Cryocrushing is another method for isolation of microfibrils. By using liquid nitrogen, the process contains freezing cellulose fibers and subject them to high shear force [11]. Grinding processes which fiber slurry passes between static grinding wheels and rotating stones (~1500 rpm) induces shear forces that can lead to fiber fibrillation and nanofiber isolation [13-15].

1.2.2 Acid hydrolysis of cellulose microfibrils

CNC can be prepared by acid hydrolysis of cellulose microfibrils [16-20]. Acid hydrolysis of cellulose microfibrils is the widely used method and convenient process to obtain single and well-defined cellulose nanocrystals supported by the fact that the preference acidic attack in the amorphous regions while crystalline regions are mostly insoluble in acids. The acid treatments are mainly using sulfuric acid, phosphoric acid and hydrochloric acid [16, 18, 21, 22]. The mainly common function of acid is their ability to release amorphous regions along the cellulose molecular chains, therefore breaking down the hierarchical structure of the nanofibril bundles into crystalline nanocrystals. After removing amorphous regions of cellulose microfibrils, the individual crystallites are eventually liberated with nanometric dimension while the crystallites remain intact aligned along the fibril's axis. After the acid treatment, the obtained cellulose nanocrystals show whisker or rod shape particles.

The sulfuric acid treatment has been widely used to extract CNC through surface reactions process [22, 23]. By using sulfuric acid as acid hydrolysis agent, the acidic sulfate groups generated would be simultaneously introduced and left on the surface of produced CNC through the esterification of surface hydroxyl groups from cellulose. Therefore, it creates the negatively charged surface above acidic pH. The negatively charged surface of the CNC creates electric double layer repulsion among the whiskers in suspension to achieve anionic stabilization. The preparation of CNC with sulfuric acid resulting in

stable colloid suspensions of well-defined CNC then those prepared hydrochloric acids [3, 21, 24]. CNC that prepared with hydrochloric acid unable to exert negative charged sulfate groups on CNC surface as evidenced by reaction scheme of below figures[25-29]. The negative sulfate groups on CNC could be determined by the FTIR since the distinct sulfate peak located at the 1205 cm^{-1} in the spectrum of the CNC represents the S=O vibrations which ascribed to the sulfate functionality.

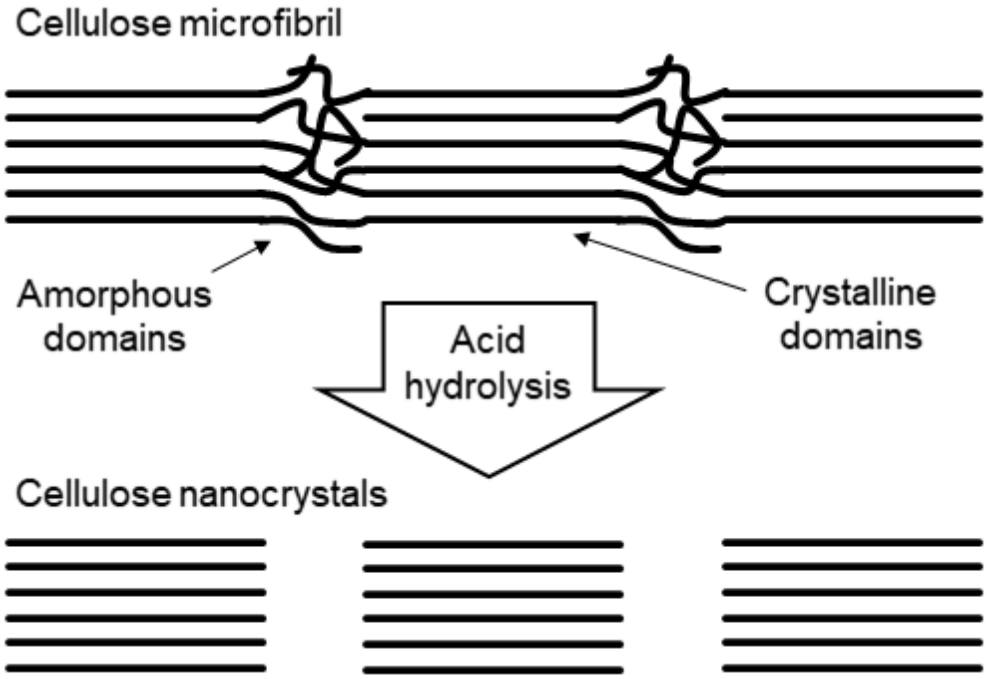

Figure 1.2 Removal process of amorphous fraction of CNC by acid treatment.

1.2.3 Mechanical properties of CNCs

Atomic force microscopy(AFM), X-ray diffraction (XRD) and Raman spectroscopy were used to calculate the elastic properties of CNC [30]. The theoretical tensile strength of CNC is in the range of 7.5-7.7 GPa [30]. The elastic modulus of CNC obtained from tunicate was determining by three-point bending test with AFM. The elastic modulus was found to be 150 GPa [31]. The mechanism of deformation of tunicate cellulose whiskers proved that the calculated modulus of tunicate CNC is 143 GPa by Raman spectroscopy [32].

1.3 Carbonization of Cellulose Nanocrystals

1.3.1 Mechanism of carbonization of cellulose

Figure 1.3 indicates the mechanism of carbonization of cellulose. Tang et al [33] reported that the pyrolysis of cellulose up to 500 °C studied by the use of infrared absorption techniques on fibers and films. Combining the results with those obtained from static thermogravimetric analysis, gas evolution data, and physical property data had permitted detailed reaction mechanisms for the carbonization process. The process consists of 4 successive stages. Step 1: desorption of physically absorbed water, Step 2: splitting off of structure water, Step 3: chain scissions or depolymerization and breaking of C-O and C-C bonds within ring units, accompanied by the evolution of more water, CO, and CO_2 and Step 4: aromatization or formation of graphite-like layers. Carbonization processes are controlled by two reactions: dehydration and depolymerization. Firstly, dehydration reaction occurs by removing the non-carbon elements in the biomass like hydrogen and oxygen by generating evaporable gases such as CO_2, CO and H_2O. Depolymerization of cellulose chain results in double bonds, conjugated double bonds and even free carbon radicals, which are participating units for the subsequent repolymerization and aromatization reactions [34].

Brunner et al [35] reported that at low temperature below 240 °C, the rate determining step is dehydration. Dehydration reaction of cellulose stabilizes the remaining carbon polymers removing the hydroxyl groups resulting in double bonds and forms aromatic structures. Dehydration at low temperature controls the cellulose decomposition by cleavage/scission at high temperature. Moreover, the result confirmed that a less stable carbon structure in the case of high heating rate and the char yield decreased with high heating rate.

Yoshino et al [36] studied the carbonization of bacterial cellulose film under Ar atmosphere depending on the heat treatment temperature. The film of HTT-2900 is well graphitized and the interlayer spacing of graphite is evaluated to be 0.356 nm. Moreover, conductivity increases remarkably with increasing temperature, tending to saturate above 1000 °C and then conductivity again increase

above HTT of 2500 °C.

Norten et al [37] found oxidation of cellulose tends to increase the surface area of the resulting char. NMR, elemental analysis, and DSC show how cellulose oxidation tends to increase aromaticity and cross-linking. The oxidation step was performed at 200 °C for varying times and then carbonization was performed at 900 °C under nitrogen atmosphere. DSC data confirmed that oxidation process decreases diffusion rates of volatiles out of the oxidized cellulose during pyrolysis, giving denser carbons and higher BET surface areas. Furthermore, oxidation encourages extensive aromatic production combined with increased cross-linking, resulting in a highly aromatic and cross-linked structure. It was confirmed Tg increased with increasing oxidation and such behavior is usually associated with increasing cross-linking or stiffening of the macromolecular chains.

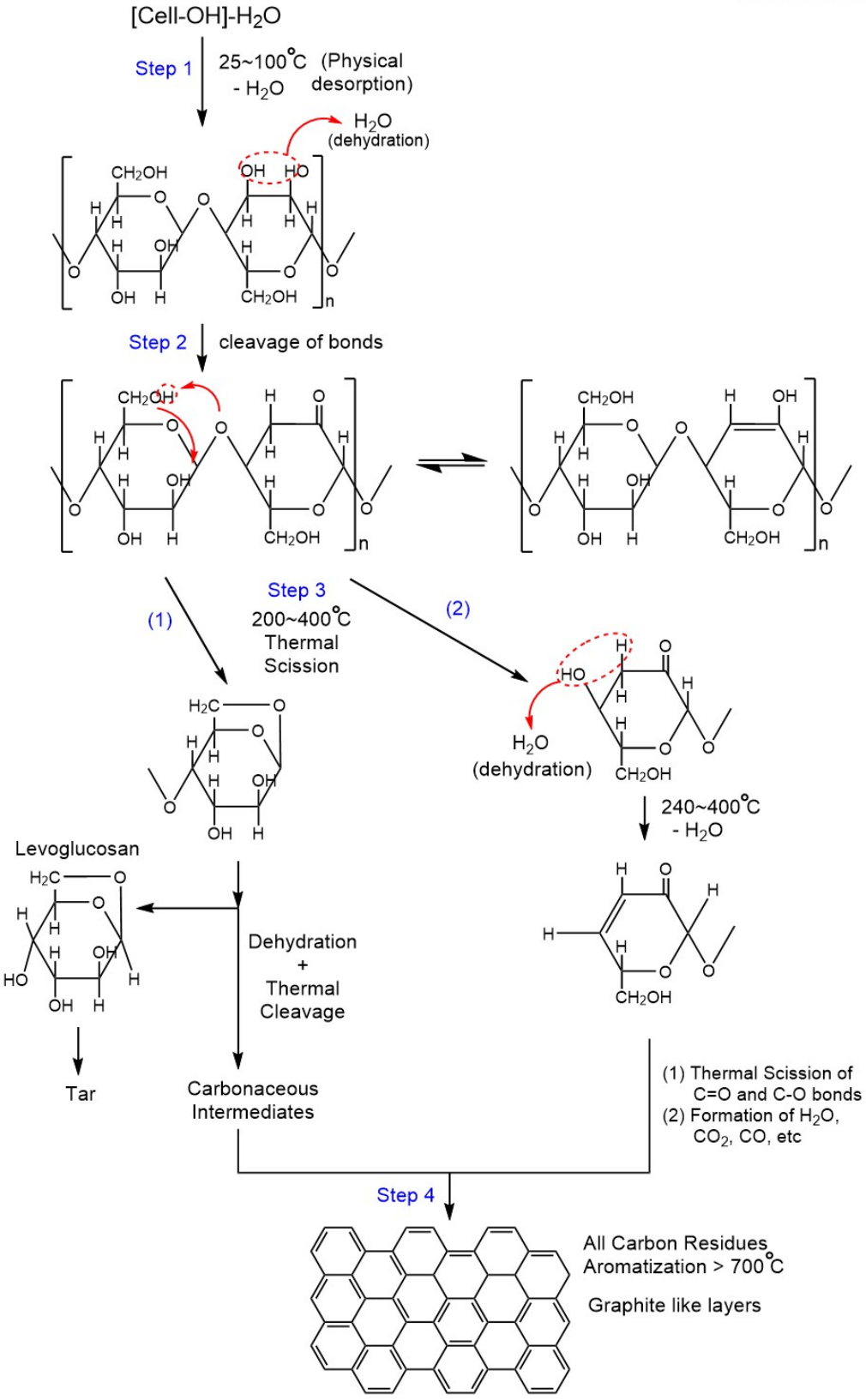

Figure 1.3 Proposed mechanism for the conversion of cellulose to carbon [33].

1.4 Polymer/CNC Composites Films and Fibers

1.4.1 Dispersion of Cellulose nanocrystals

Due to hydrogen bonding and van der Waals force between the chains, dispersion of CNC is one of the key parameters as a reinforcing agent [20, 38]. The ultrasonication is an ideal isolation method due to high efficiency, low costs and ability to facilitate dispersion of the CNC in the suspension. The principle of ultrasonication is the conversion of ultrasound energy to a hydrodynamic force of ultrasonic waves through the process of formation, growth, and collapse of cavities in water suspension. The potential energy of bubble is transformed into the kinetic energy of a liquid get and it causes the breakage of weak bonding among the CNC aggregates in the suspension. With increasing power and time of sonication, the CNC become more dispersive, and it is desirable to produce the composite with better uniformity of CNC [38].

There are two types of sonication, one is bath-type sonication (indirect sonication) and the other is horn-type sonication (direct sonication). In bath sonication, the ultrasonic waves pass through the bath liquid and the wall of sample container before reaching the suspension. Whereas, in case of horn sonication, the ultrasound probe or horn is immersed directly into the suspension. Horn sonication is normally used for dispersing dry powders due to higher effective energy output into the suspension. Bath sonication is used for re-suspension of samples or the samples which might be damaged under horn sonication[39].

Dong et al [39] conducted ice bath sonication with different treatment times. The suspension samples acquired by sulfuric hydrolysis at 45 °C for 1hr. Long duration treatments were performed in 20 min segments with intermediate cooling intervals. The particle size decreased during the first 5 min of ultrasonication, but there was no significant change after 5 min.

Chang et al [40] studied the degree of dispersion of individually dispersed wood-based CNC in solvents including DMF, H_2O and a mixture of H_2O/DMF was confirmed by changing sonication time and contents of moisture-containing CNC. Upon using the equation (1), they can obtain the hydrodynamic radius of CNC after sonication.

$$D_h = L/\ln(L/d) \quad (1)$$

The hydrodynamic radius of CNC was calculated to be between 22 and 27 nm by equation (1) when CNC dispersed individually in H_2O/DMF solvent. At the moisture content of 3.8 wt.%, hydrodynamic radius of 23 nm was achieved after 24 h sonication. They suggested that the moisture

significantly affects the dispersibility of CNC in DMF. With the moisture containing CNC, hydrogen bond forms between water and CNC surface and thus it weakens the interaction between the CNC. Therefore, the moisture containing CNC results in better dispersion than CNC without moisture.

1.4.2 CNC related polymer nanocomposites

CNC has been widely used as fillers or reinforcing materials for polymer nanocomposites to improve thermal properties or mechanical properties due to its specific modulus, stiffness, and high aspect ratio[31, 32].

For the first time, Favier et al [29, 41]. reported CNCs for reinforcing poly(S-co-BuA). They found a spectacular improvement in the storage modulus measured by dynamic mechanical analysis, above the glass-rubber transition temperature range, even at 6% weight fraction of CNC. George et al [42] processed CNC improved thermal stability of PVA and mechanical properties even the addition of low concentration of CNC. More than 100% improvement of tensile strength was noticed by the incorporation of 4 wt.% of CNC. CNC was embedded into polylactide-polyglycolide and nanocomposites whose superior thermal stability, mechanical properties [43]. Favier et al reported that incorporation of 6 wt.% of CNC increased by more than three orders of magnitude in the rubbery state of polymer matrix [41]. Libo et al [44] conducted the ABS/CNC nanocomposites. Only 0.7 wt.% of CNC in the composite was enough to increase the tensile strength and modulus. Moreover, the storage modulus of ABS/CNC7 in the glassy stage was 3.68 GPa about 54% higher than pure ABS (2.39 GPa). PP/CNC nanocomposites have the tensile strength of the composite compared with neat PP improves by 70-80% with the addition of CNC. The crystallinity has also been improved by about 50% in the CNC reinforced samples. As the content of CNC increases, the composites exhibit higher thermal degradation temperature, higher hydrophilicity and higher thermal conductivity [45].

Chapter II. Structural analysis of carbonized cellulose nanocrystals

2.1 Introduction

2.1.1 Carbonization of cellulose nanocrystals

CNC is one of the promising precursors for carbon materials. CNC can be obtained from various resources such as tunicate, marine animals, algae and fungi [1, 3, 7]. The well-organized CNC has attentions due to high aspect ratio and high mechanical properties. In addition, the high crystallinity and structural order of CNC make them a potential precursor for graphite structure as compared to other cellulose-based carbon materials [46].

Ordered CNC has been transformed into porous carbon with an increased short-range ordered lattice and percolated carbon nanofibers at 1000 °C with stabilization step [47]. The pyrolysis of the freeze-dried CNC was stabilized at 250 °C in air and carried out under a nitrogen atmosphere at 300-1000 °C and carbons obtained at different temperature indicate the presence of well-organized and more defective carbons, respectively [48]. Electro-spun cellulose nanofibers were stabilized at 240 °C in air for 1hr and then carbonized in the range of 800-2000 °C [49]. From these papers, there are no discussions of how oxidative stabilization process affects structural development of CNC-based graphite. In this study, we have conducted experiments to study the effect of oxidative stabilization process on the structural development of CNC-based graphite.

2.2 Experimental

2.2.1 Materials

Spray-dried CNC was purchased from the University of Maine. The dimension of CNC reported by supplier was 5-20 nm in diameter and 100-200 nm in length.

2.2.2 Carbonization condition and sample codes

CNC was carbonized at a heating rate of 5 °C/min and flow rate of 2 L/min. The tube furnace (Nashiltech, Korea) was used to perform carbonization process.

A. D-cCNC X: Direct carbonization samples were heated at a desired temperature from 1000 to 2500 °C under an inert atmosphere at a heating rate of 5 °C/min. X represents the carbonization temperatures.

B. S-cCNC X: The samples were heated from room temperature to 250 °C in air at a heating rate

of 5 °C/min and held at 250 °C for 1 hr followed by heating at the desired temperature up to 2500 °C under an inert atmosphere at a heating rate of 5 °C min^{-1}. X represents the carbonization temperatures.

2.2.3 High-resolution Transmission Electron Microscopy (HR-TEM)

To examine the detailed structure with different carbonization condition, TEM images were obtained using a Tecnai G2 F20X Twin. The samples were dispersed in DMF with 0.05 wt.% concentration by using horn-type sonication for 4 hr. The images analyzed by the Digital-Micrograph tool.

2.2.4 Raman Spectroscopy

Raman spectra were measured using an Alpha 300s micro Raman spectrometer (WITec) equipped with a 532 nm laser. Raman spectra were collected over 30 sites of samples and were averaged over thirty scans to improve the signal to noise ratio and the data were corrected for the spectral response of the instrument. Raman curve fitting for the determination of spectral parameter was performed with the software program called by Peakfit software package supplied by sigmaplot.

2.2.5 WAXD Analysis

X-ray diffraction (XRD) analysis (Bruker D8 Advance, Germany) with Cu-Kα radiation (λ=1.54056 Å).

2.2.6 X-ray Photoelectron Spectroscopy

X-ray photoelectron spectroscopy (ESCALAB 250XI, Thermo Fisher Scientific, USA) was used to investigate the composition of sp^2 and sp^3. The assignments of C_{1S} peak component shown in Table 2.5 [50-52]. The peak analysis was performed by means of the peak deconvolution to fit a Gaussian function by the origin-peak fitting program.

2.3. Result and Discussion

2.3.1 Carbonization behavior of CNC

Carbon yield of CNCs at a given heat treatment temperature and their samples codes are listed in Table 2.1. The char yield of D- and S-cCNCs obtained from higher carbonization temperature give lower carbon yield resulting from the removal of amorphous carbon and disordered carbon. Carbon yield of D- and S-cCNCs have similar value at each carbonization temperature. The result suggests that stabilization process does not have a significant effect on the carbon yield.

Table 2.1 Sample code and carbon yield of carbonized CNC

	Sample code	Carbonization temperature (°C)	Yield (%)
With stabilization (@250 °C for 1 hr)	S-cCNC1000	1000	23.5
	S-cCNC1500	1500	20.6
	S-cCNC2000	2000	14.4
	S-cCNC2500	2500	12.3
Without stabilization (Direct carbonization)	D-cCNC1000	1000	18.1
	D-cCNC1500	1500	18.6
	D-cCNC2000	2000	16.1
	D-cCNC2500	2500	15.8

TEM Figure 2.1 represent HR-TEM images of D and S-cCNC at various temperature conditions. S-cCNC samples show whisker structure retaining their original structure whereas D-cCNC result in fused bulk carbon structure. Figures 2.1 (e-h) show the highly oriented structure of carbonized CNC with 5-10 nm in diameter and 50-100 nm in length. It can be assumed that dimension of S-cCNC samples are reduced by the heat-treatment. For D-cCNC, fused carbon structure with large size samples are shown in Figures 2.1 (a-d). The high magnification images of D- and S-cCNCs are shown in Figure 2.2. As the temperature increase, D-cCNCs with large crystal size are formed which is indirect evidence for the fusion of CNC during heat-treatment. For S-cCNCs, the dimension of whisker decreases with increasing carbonization temperature. S-cCNCs indicate the development of graphitic structure even at 1000 ^{o}C and form the highly-ordered structure with a little defect, while D-cCNCs were mostly disordered carbon at the same temperature. The *d*-spacing of D- and S-cCNCs are plotted in Figure 2.3. The perfectness of graphitic structure increase with increasing carbonization temperature. At whole temperature, *d*-spacing of S-cCNC is smaller than that of D-cCNC. In case of, *d*-spacing of S-cCNC1000 and D-cCNC have 0.345, 0.368, respectively. For D-cCNC samples, the experimental data prove the formation of graphitic carbon structure above 2000 ^{o}C carbonization temperature. S-cCNC samples the exhibit similar value of theoretical *d*-spacing of graphite. It suggests that stabilization process help CNC to make well-defined graphite structure development. Norten et al [37] found that oxidation process of the cellulose gives dehydration of the cellulose gives dehydration of the cellulose, resulting in the aromatic formation and crosslinking of the structure. Furthermore, oxidation encourages extensive aromatic production combined with increased crosslinking resulting in a highly aromatic, highly crosslinked network. For S-cCNC samples, the activation energy needed for graphitization is relatively lower than D-cCNC samples. Therefore, the graphitization process occurs at a relatively low temperature and the high graphitic perfectness and low amorphous content are well-established at low temperature.

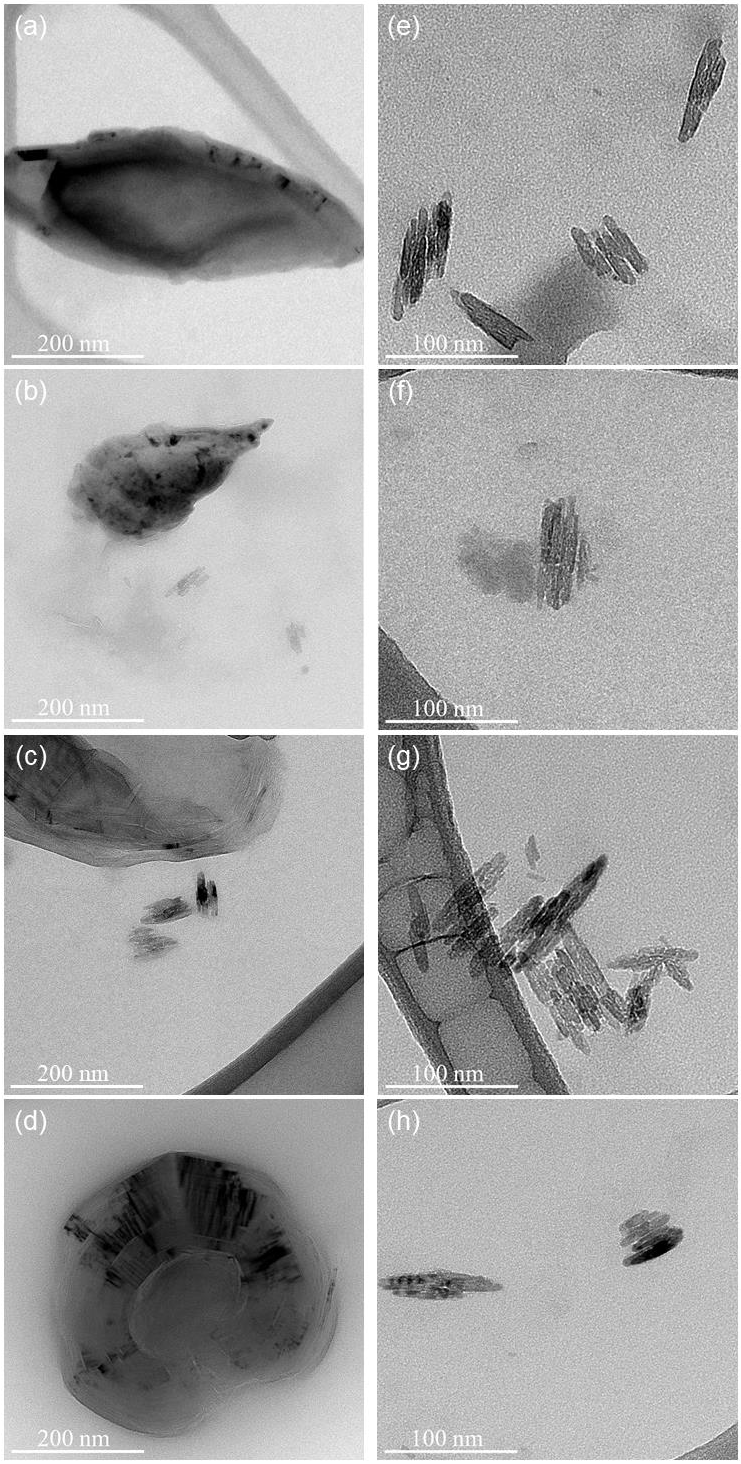

Figure 2.1 High resolution Transmission Electron micrographs (HR-TEM) of D-cCNC and S-cCNC; (a) D-cCNC1000, (b) D-cCNC1500, (c) D-cCNC2000, (d) D-cCNC2500, (e) S-cCNC1000, (f) S-cCNC1500, (g) S-cCNC2000 and (h) S-cCNC2500.

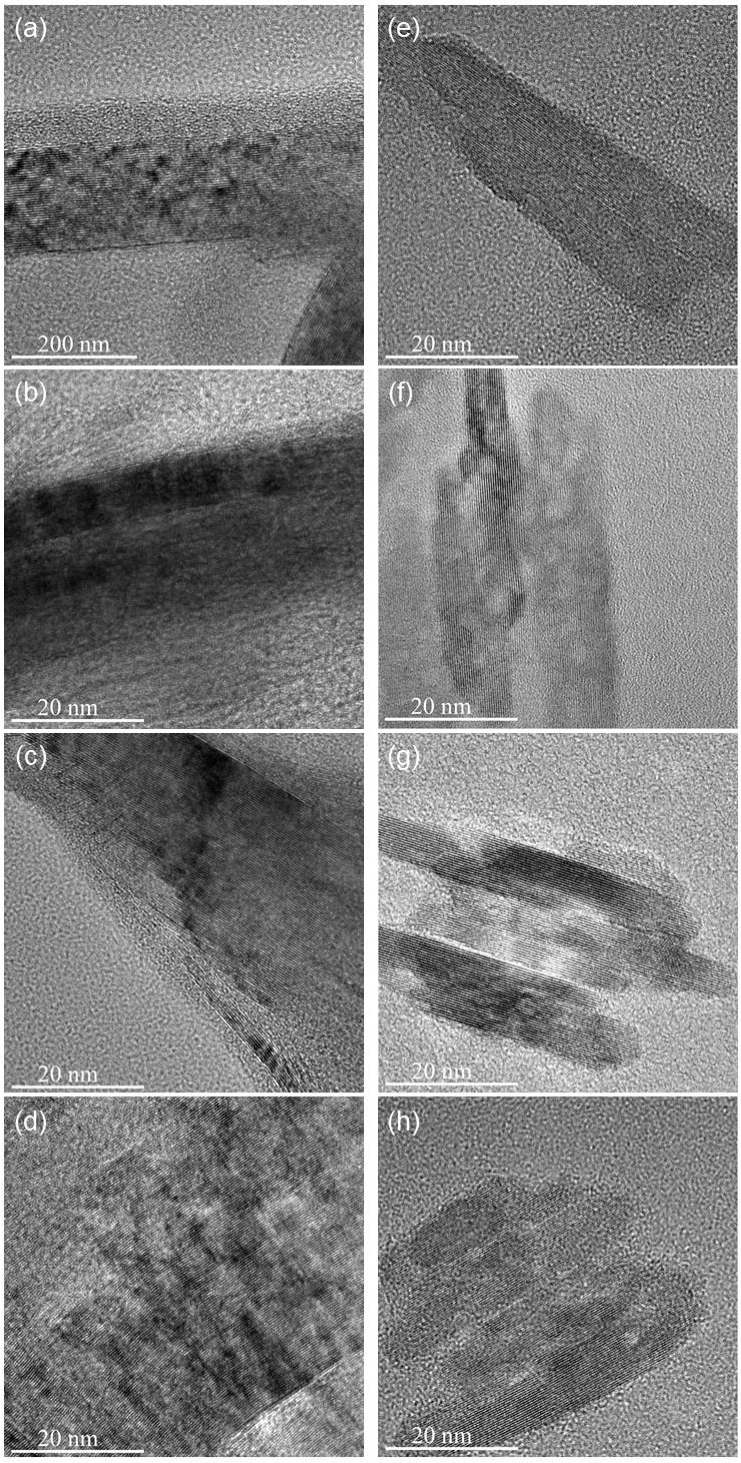

Figure 2.2 HR-TEM of D-cCNC and S-cCNC; (a) D-cCNC1000, (b) D-cCNC1500, (c) D-cCNC2000, (d) D-cCNC2500, (e) S-cCNC1000, (f) S-cCNC1500, (g) S-cCNC2000 and (h) S-cCNC2500.

Fusion sequence of directly carbonized CNC during heat treatment is schematically shown in Figure 2.4. D-cCNCs exhibit the fused carbon structure. Figure 2.4 (a) suggests that fusion point occurs in the end-end part of the samples and forms a fused bulk carbon structure. Figure 2.4 (b) shows that fusion occurs along the boundary of samples and interface of samples. Figure 2.4 (c) indicates linked structure between boundary and lead to form large and thick crystal sample. Figure 2. 4 implies that fibrillar structure of pristine CNC was transformed into the irregular structure by molecular fusion during direct carbonization process. For S-cCNCs, stabilization process helps CNC create active sites at the early stage of carbonization process. From the active site, the crystal structures are formed and the crystal size of S-cCNC is small due to lots of active sites. Since there is no stabilization process for D-cCNC samples, initially there are few active sites and finally grow to a carbon structure with a large crystal size. Figure 2.5 represents the high magnification images of D- and S-cCNCs to observe the microstructure. The number of defect sites per selected area is analyzed in Figure 2.6. In both samples, kink sites and distortion sites can be observed in Figure 2.5. As shown in Figure 2.5 (a-d), due to the fusion behavior, there are lots of kink sites and distortion sites. Relatively, S-cCNCs have fewer defects and distortion sites than D-cCNCs. The number of defects is small in the S-cCNCs compared to the D-cCNCs. It can be confirmed that the number of defects is reduced with increasing carbonization temperature.

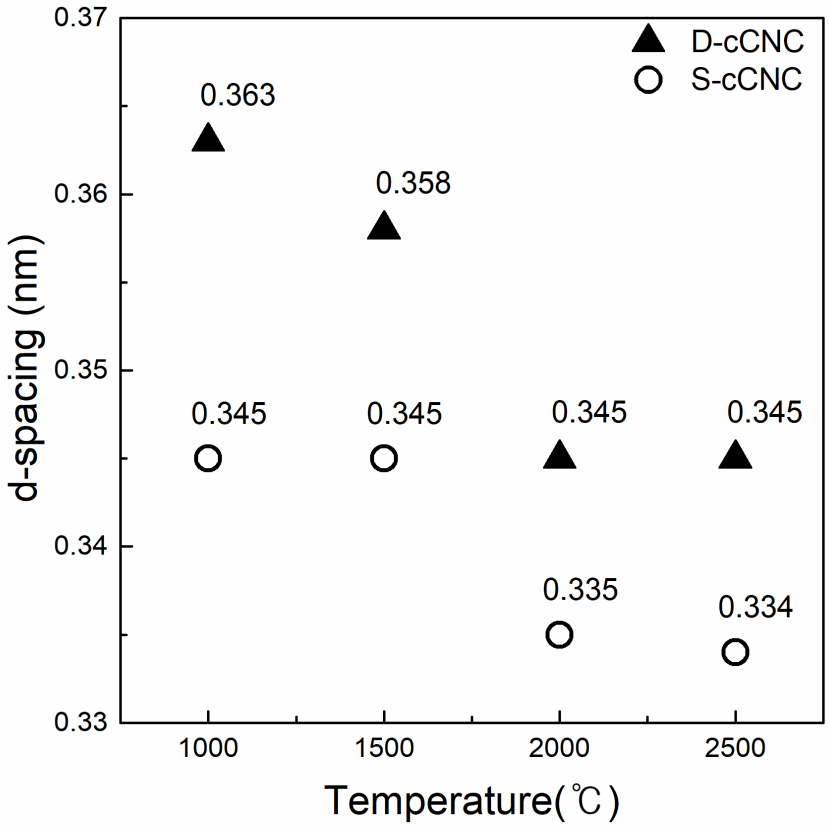

Figure 2.3 *d*-spacing of carbonized CNC from TEM photographs.

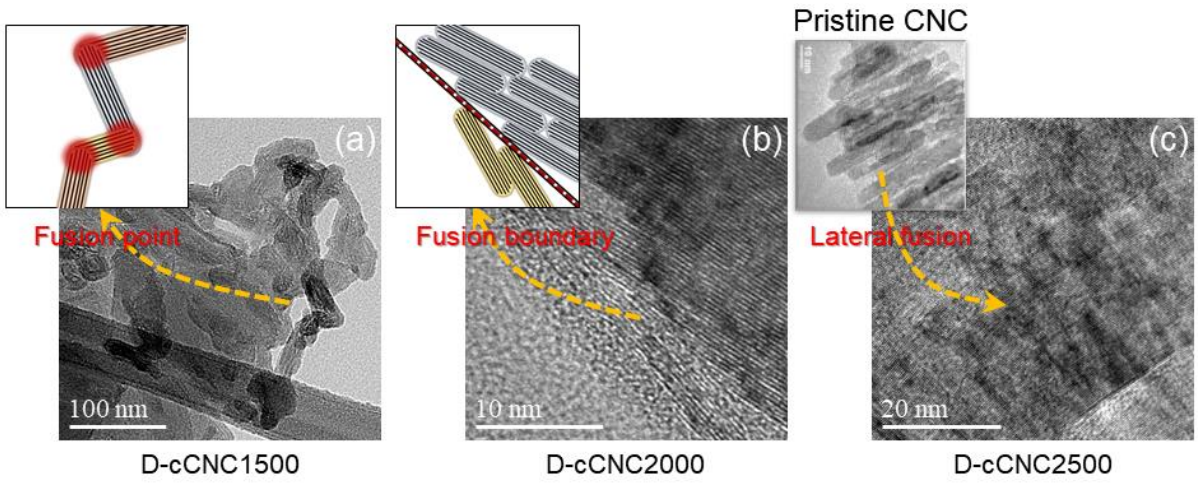

Figure 2.4 HR-TEM images of fusion sequence of directly carbonized CNC (a) D-cCNC1500, (b) D-cCNC2000 and (c) D-cCNC2500. Each inset image indicates the structural development depending on carbonization temperature.

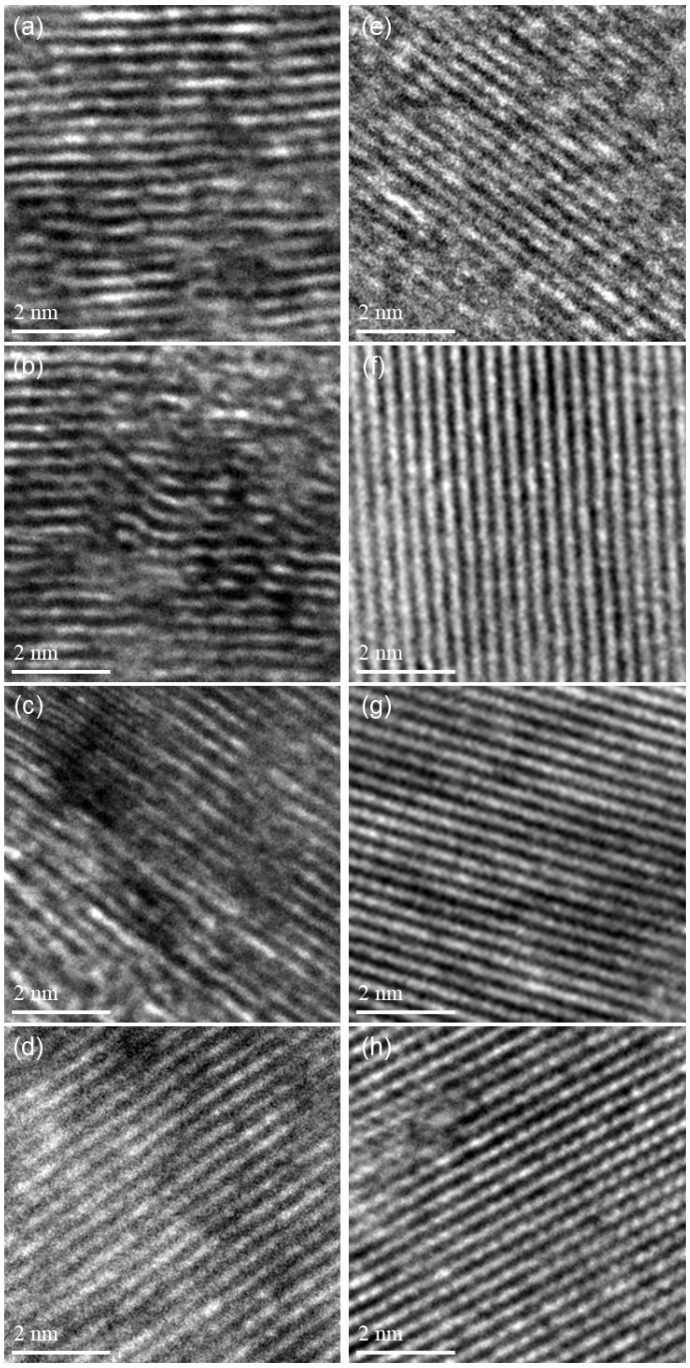

Figure 2.5 HR-TEM images of (a) D-cCNC1000, (b) D-cCNC1500, (c) D-cCNC2000, (d) D-cCNC2500. HR-TEM images of (e) S-cCNC1000, (f) S-cCNC1500, (g) S-cCNC2000, (h) S-cCNC2500.

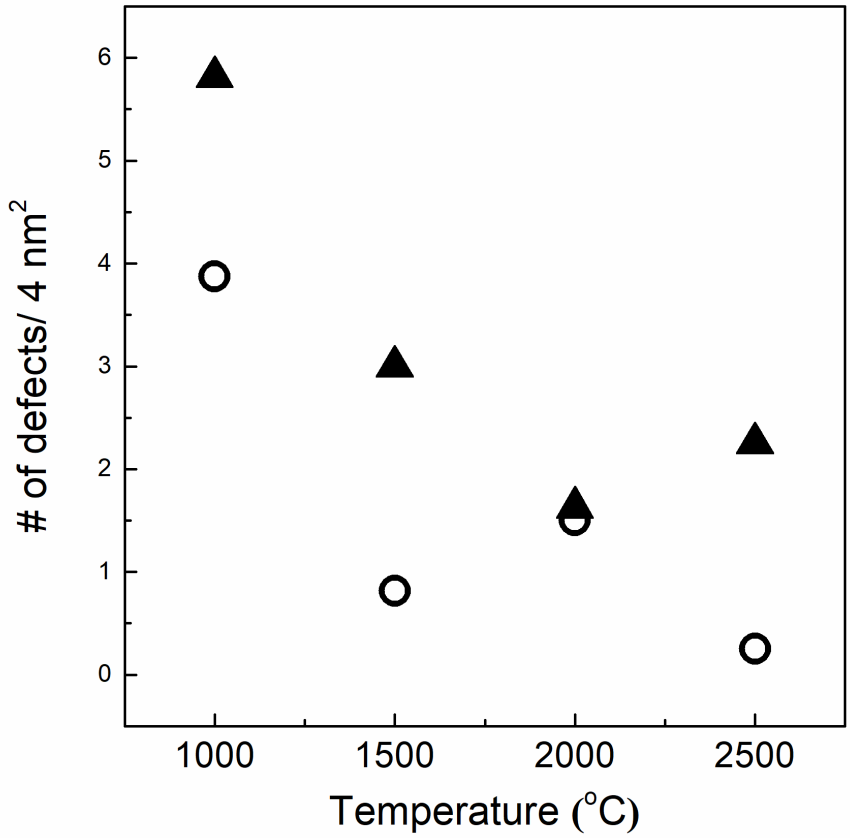

Figure 2.6 The number of defects /4 nm^2 of carbonized CNC from TEM photographs.

2.3.2. Structural characterization of carbonized CNC

Raman spectroscopy is a powerful tool to analyze the degree of the perfectness of graphitic structure for various carbon materials including highly oriented pyrolytic graphite (HOPG), graphene, carbon nanotubes, pyrocarbons or carbon black [53-62]. It is well known that the Raman spectra provide information on the crystalline perfection of graphite-based materials. Raman spectrum of single-crystal graphite and HOPG shows a single band at 1580 cm^{-1} and is indicative of the ordered crystallites of the carbons. Disordered graphitic lattice from graphene layer edges shows a single band at 1350 cm^{-1}. Disordered graphitic lattice from surface graphene layer shows a single band at 1620 cm^{-1} (D'). Amorphous carbon appears at 1500 cm^{-1}. Disordered graphitic lattice, polyenes, ionic impurities structure indicates at 1200 cm^{-1} and the band called transpolyacetylene (TPA). Amorphous carbon band locates on 1503-1534 cm^{-1}. The spectra were analyzed using a mixed Gaussian-Lorentzian curve fitting procedure, to obtain the best curve fitting with 4 bands at 1180-1200 cm^{-1} (TPA), 1345-1350 cm^{-1} (D band), 1503-1534 cm^{-1} (A band) and 1580-1600 cm^{-1} (G band), respectively [63-70]. After heat treatment at 2400 ^{o}C, D' peak appears at 1620 cm^{-1} and 5 bands are used to obtain best curve fitting

Figure 2.7 shows the Raman spectra of D- and S-cCNCs. The spectra are normalized to the maximum value of the intensity of the G band located in every case at around 1580-1600 cm^{-1}. The positions of the bands are invariant with temperature. From the Raman spectra, the peak separation of G band and D band is clearly observed. Separation of G and D band are clearly observed by heat treatment process and the peaks are also sharpened. It is interestingly noted that I_G/I_D ratio of D-cCNC2400 dramatically increase. The structural difference between D- and S-cCNCs were analyzed by peak fitted data (Figure 2.8). G band (1580 cm^{-1}), D band (1345 cm^{-1}), TPA band (1200 cm^{-1}) and A band (1503-1534 cm^{-1}) were used until carbonization temperature 2200 ^{o}C. After heat treatment at 2400 ^{o}C, for D-cCNC2400,2500 and S-cCNC2400, 2500, 5 bands were used to progress the peak fitting. Fitted data are summarized in Table 2.2 and 2.3, respectively. Variation of I_G/I_D, A_G/A_D, FWHM G and A_A with temperature are plotted in Figure 2.9. Figure 2.9 (a) indicates the variation of the intensity ratio (I_G/I_D) of raw data and fitted data. Fitted data of I_G / I_D for S-cCNC samples are almost constant below 2000 ^{o}C, but tend to increase above 2000 ^{o}C. The Maximum value of I_G / I_D at 2500 ^{o}C is 1.0. S-cCNC samples of I_G / I_D does not show a large variation. The ratio slightly increases with increasing carbonization temperature. Fitted data of I_G / I_D for D-cCNC samples seem no significant difference. However, for D-cCNC2400 and 2500, the value of I_G / I_D is 6.6 and 4.5, respectively. The data represents the formation of graphitic structure. Both D-cCNC2400 and 2500 samples have high standard deviation. In the carbonization process, D-cCNCs formed fused carbon structure with large crystal size and the irregular large crystal is caused by the difference in the degree of carbonization partly.

Figure 2.9 (b) represents A_G/A_D spectra of D- and S-cCNC samples. The ratio of A_G/A_D indicates the degree of graphitization of samples. For both samples, the ratio of A_G/A_D increase with increasing carbonization temperature. A_G/A_D for S-cCNC samples indicate that the value increase with temperature from the 1800 °C and the maximum value of A_G/A_D is 1.0 at 2500 °C. Moreover, the fitted data of A_G/A_D for D-cCNCs exhibit the maximum value of 3.6 at 2400 °C.

Figure 2.9 (c) represents the FWHM of G band. FWHM G band directly related to the structural disorder presents, since it arises due to the distortions in bond length and bond angle [71, 72]. It tends toward zero if cluster formed defect-free and unstrained like pure graphite. Table 2.3, 4 and figure 2.9 (c) gradually decrease with increasing carbonization temperature. The broader the band, the small crystal are formed and have large defect sites. As the temperature increases, defect sites inside in the samples are reduced and crystal size are increased. D-cCNC 2500 has the value of 26.4 cm^{-1}, which is similar to the graphite of 15 cm^{-1}. It represents highly oriented graphitic structure formed. S-cCNC samples has more than double (40.2 cm^{-1}) that of graphite. As in-plane defects and small cluster size are both known to broaden G band, these trends suggest the level of defects is decreasing and/or the lateral dimensions of the clusters are increasing along the annealing pathway. The fraction of amorphous are is plotted in Figure 2.9 (d). The percent of the amorphous fraction for both samples decrease with increasing carbonization temperatures. The result is ascribed that the structural conversion from disordered carbon and amorphous carbon by removal of amorphous carbon.

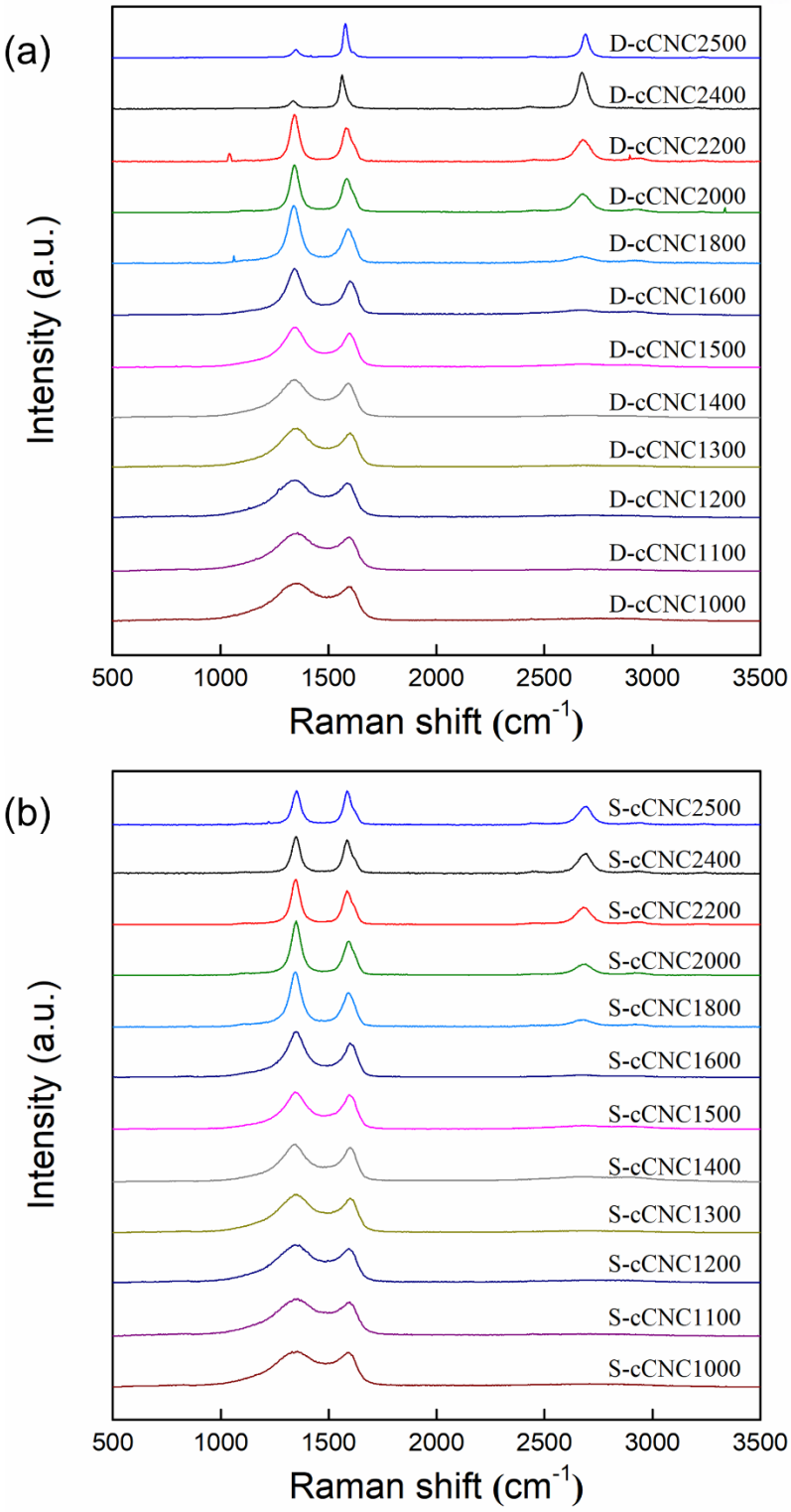

Figure 2.7 Raman spectra of (a) D-cCNC and (b) S-cCNC.

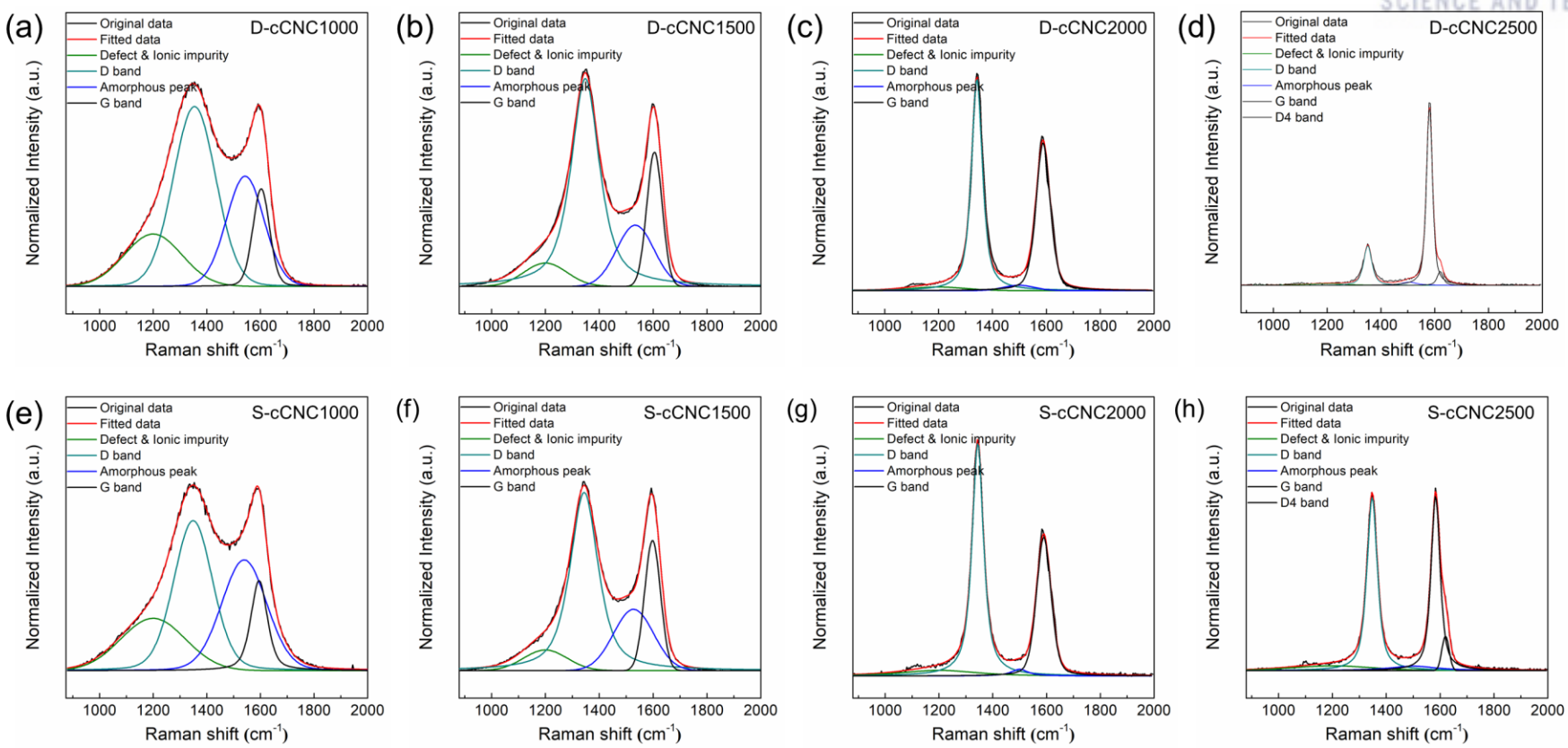

Figure 2.8 Fitted Raman spectra based on five kinds of bands for (a) D-cCNC1000, (b) D-cCNC1500, (c) D-cCNC2000 (d) D-cCNC2500 (e) S-cCNC1000 (f) S-cCNC1500 (g) S-cCNC2000 and (h) S-cCNC2500.

Variation of $I_A/I_{G,}$ G band position, crystal size and I_{TPA}/I_G with temperature are presented in Figure 2.10. I_A/I_G of D- and S-cCNCs are plotted in figure 2.10 (a). A band associated with disordered carbon including various carbon structures such as carbon blacks, activated carbon, carbon onions, diamond-like carbon films and graphene [73, 74]. I_a band is related to two different types of defects. Firstly, the band is associated with sp^3 interstitial sites attached to the sp^2. Secondly, it represents sp^2 based point-like defects, in particular, non-hexagonal rings. As shown in Figure 2.6 and 2.7 (TEM), they are observable distortion sites and kink sites at low carbonization temperature (1000 and 1500 °C). TEM and Raman spectroscopy evidenced graphitic structure with low perfectness formation in the D- and S-cCNCs. Defects are hardly found above 2000 °C by TEM (Figure 2.6 and 2.7). Furthermore, the value of I_a close to zero with both samples which means that this point-defect like structures disappeared and the graphitic structure are formed. The Position of G band is plotted in Figure 2.10 (b). The position of G band position move downshift with increasing carbonization temperature toward 1580 cm^{-1}. This trend also represents an increasing degree of graphitization along the annealing temperature.

Furthermore, In Raman spectroscopy studies on carbon materials, the Tuinstra-Koening [55] was often employed to estimate crystal size by correction.

$$L_{a=(}2.4 \times 10^{-10})\ \lambda_l^{10}\ (I_G/I_D) \qquad (2)$$

Crystal size for D- and S-cCNCs are shown in Figure 2.10 (c). The crystal size is calculated by Tuinstra-Koeing law. The crystal size of both samples has approximately 11.5 nm below 2000 °C. Above the 2000 °C, the crystal size of both samples graudally increase. However, in case of D-cCNC2400 and D-cCNC2500, the crystal sizes are 126.9 and 86.5 nm, respectively. S-cCNC2400 and S-cCNC2500 have the value of 17.3 and 19.2 nm, respectively. The result also confirmed that D-cCNC samples have larger crystal size than S-cCNC samples. HR-TEM and Raman spectroscopy evidence the difference of crystal size of D-cCNC and S-cCNC. Furthermore, it also clarifies that fusion sequence of D-cCNC samples (Figure 2.4). Figure 2.10 (d) shows the I_{TPA}/I_G as a function of carbonization temperature from 1000 to 2500 °C. TPA band intensity also tends to decrease with increasing carbonization temperature. Raman spectroscopy data clarifies that the graphitic structures are gradually developed with increasing carbonization temperature through structural conversion from disordered or amorphous carbon regions. Fitting results of Raman spectra informed that increase of carbonization temperature resulted in the decrease of the content of amorphous carbon. Furthermore, the graphitic structure was developed with increasing carbonization temperature through structural conversion from disorderd amorphous carbon regions.

G band (1580 cm^{-1}) and D band (1355 cm^{-1}) was used to determine graphitic structures. Investigation of the lengthening of the C-C bond due to thermal expansion plays an important role in the observed Raman shift with temperature [75-78]. Dependence of G bands frequencies on temperature is presented in Figure 2.11. The frequency downshift of the G band is associated with lengthening of the C-C bond [68, 79, 80]. The steeper the slope of the line, the greater the thermal conductivity of the samples [80]. The longer bond length resulted from the thermal expansion of the material upon the temperature increases. D-cCNC1500 and S-cCNC1500 show the similar slope, but s-cCNC1500 is steeper than D-cCNC 1500. The result suggests S-cCNC1500 has highly ordered structure than D-cCNC1500. Moreover, S-cCNC 2500 samples show the higher slope than D-cCNC 2500. It is indicative that a well-ordered structure of the sample has higher G band shift, which means that the sample is better able to transfer heat.

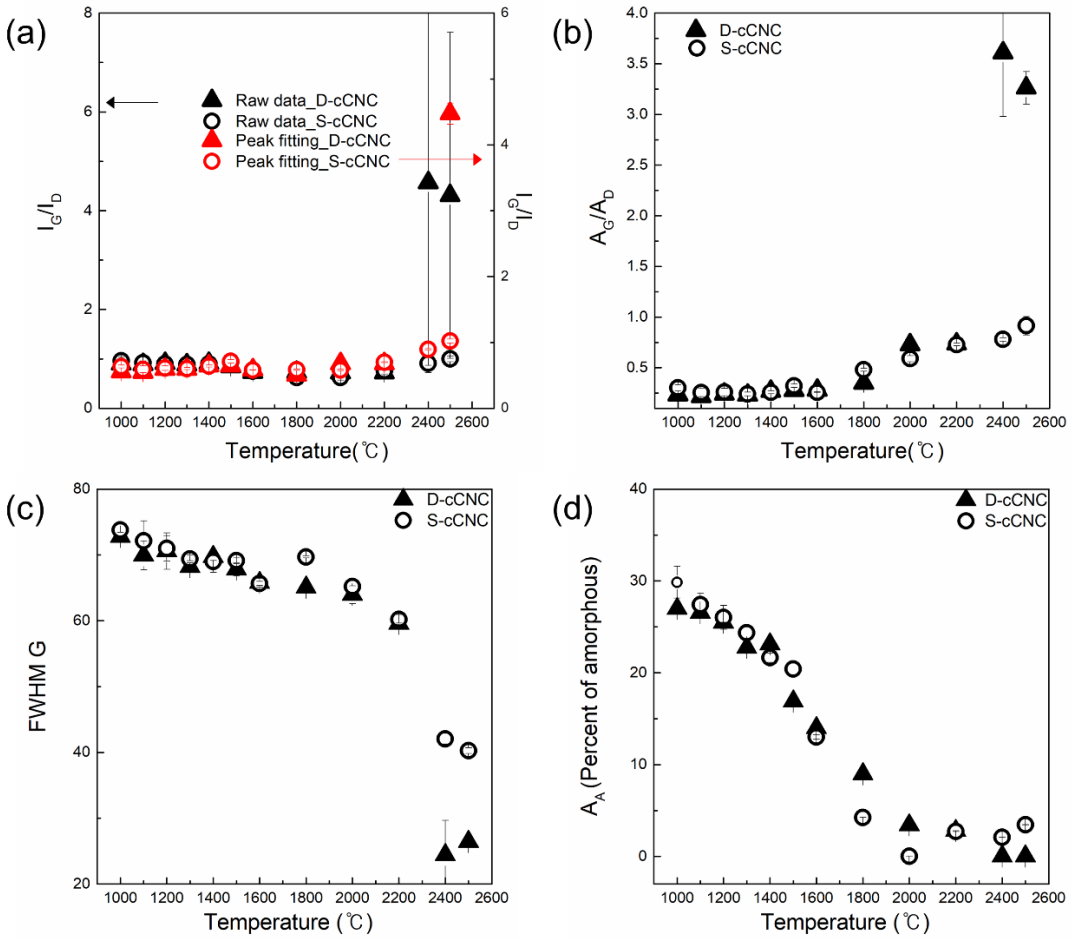

Figure 2.9 Plots of the structural parameters as a function of heat treatment temperature obtained from Raman spectra. (a) Variation of the I_G/I_D for the carbonized CNC. Black and red symbols represent the values obtained from the raw and fitted spectra, respectively. Circle and triangle symbols show fitted data of direct carbonization and with stabilization samples, respectively. (b) A Ratio of A_G/A_D band, (c) FWHM of G band of the Raman lines for carbonized CNC and (d) percent of amorphous as a function carbonization temperature.

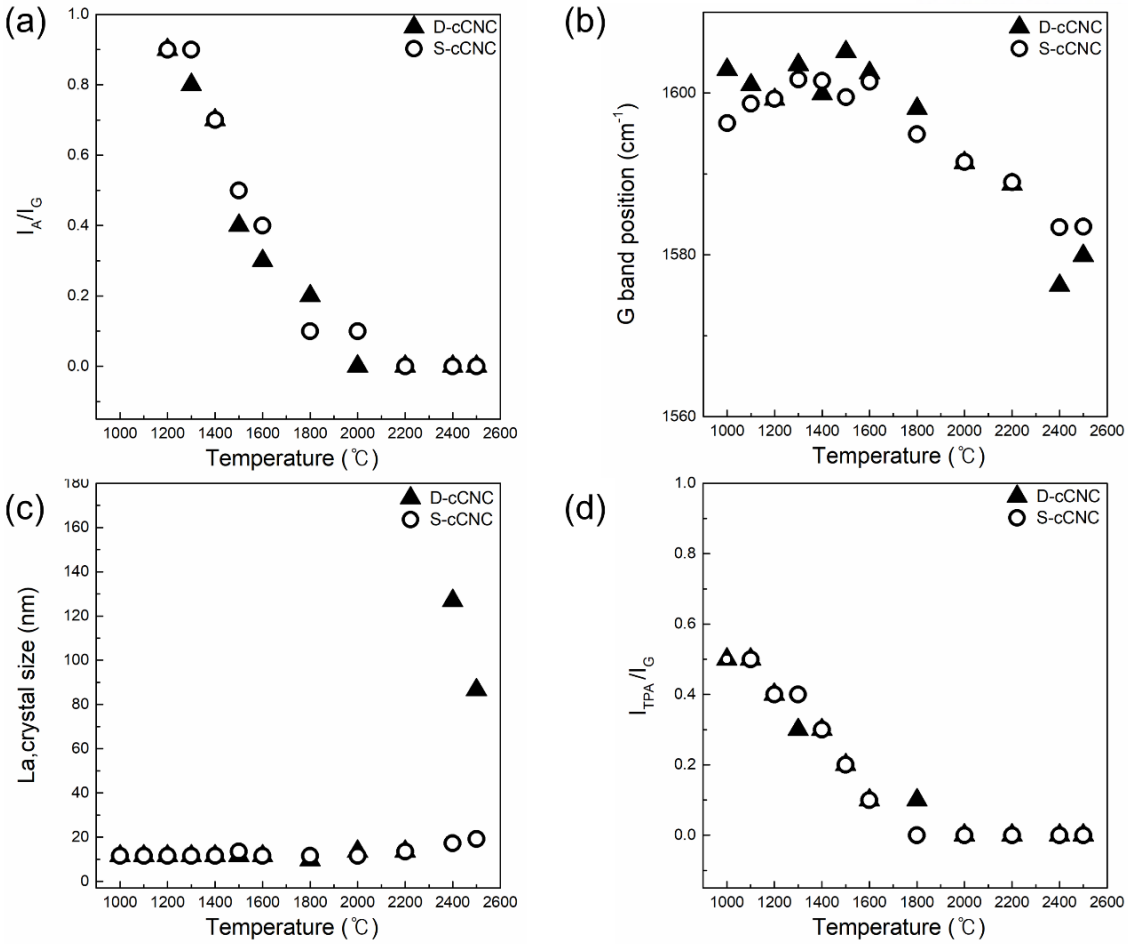

Figure 2.10 Plots of the structural parameters as a function of heat treatment temperature obtained from Raman spectra. (a) Variation of the I_A/I_G for the carbonized CNC. Circle and triangle symbols show fitted data of S-cCNC and D-cCNC, respectively. (b) G band position, (c) $L_{a,}$ crystal size, and (d) I_{TPA}/I_G band.

Table 2.2 Structural parameters from Raman spectra of D-cCNC samples

Sample code	Ratio of I_G/I_D	Fitted I_G/I_D	Area A_G/A_D	Amorphous percent (%)	FWHMG	L_a (nm)	G (cm^{-1})	TPA (1200 cm^{-1})	A (1500 cm^{-1})
D-cCNC1000	0.9±0.0	0.6±0.0	0.2±0.0	27.0±1.5	72.8±0.6	11.5	1602.9	0.5	1.1
D-cCNC1100	0.9±0.0	0.6±0.0	0.2±0.0	26.6±1.0	69.9±2.2	11.5	1601.0	0.5	1.1
D-cCNC1200	0.9±0.0	0.6±0.0	0.2±0.0	25.5±1.4	70.6±2.8	11.5	1599.2	0.4	0.9
D-cCNC1300	0.9±0.0	0.6±0.0	0.2±0.0	22.8±0.6	68.2±0.9	11.5	1603.5	0.3	0.8
D-cCNC1400	0.9±0.0	0.6±0.0	0.3±0.0	23.1±0.4	69.7±0.6	11.5	1599.9	0.3	0.7
D-cCNC1500	0.8±0.0	0.6±0.0	0.3±0.0	16.9±0.7	67.8±1.0	11.5	1605.1	0.2	0.4
D-cCNC1600	0.7±0.1	0.6±0.0	0.3±0.0	14.0±0.9	65.8±0.7	11.5	1602.5	0.1	0.3
D-cCNC1800	0.7±0.1	0.5±0.0	0.4±0.0	9.0±0.6	65.1±0.4	9.6	1598.1	0.1	0.2
D-cCNC2000	0.7±0.1	0.7±0.0	0.7±0.0	3.4±0.6	63.9±1.4	13.5	1591.4	0.0	0.0
D-cCNC2200	0.7±0.1	0.7±0.0	0.7±0.0	2.8±0.0	59.6±0.1	13.5	1588.7	0.0	0.0
D-cCNC2400	4.6±7.5	6.6±2.2	3.6±0.6	3.3±0.0	24.4±5.2	126.9±42.3	1576.2	0.0	0.0
D-cCNC2500	4.3±6.7	4.5±3.0	3.3±0.2	3.4±2.3	26.4±0.6	86.5±1.9	1579.9	0.0	0.0

Table 2.3 Structural parameters from Raman spectra of S-cCNC samples

Sample code	Ratio of I_G/I_D	Fitted I_G/I_D	Area A_G/A_D	Amorphous percent (%)	FWHMG	L_a (nm)	G (cm^{-1})	TPA (1200 cm^{-1})	A (1500 cm^{-1})
S-cCNC1000	1.0±0.1	0.6±0.0	0.3±0.0	30.0±1.7	73.8±1.0	11.5	1596.3	0.5	1.1
S-cCNC1100	0.9±0.0	0.6±0.1	0.3±0.0	27.0±1.2	72.1±3.0	11.5±1.9	1598.7	0.5	1.1
S-cCNC1200	0.9±0.0	0.6±0.0	0.3±0.0	26.0±1.3	71.0±1.9	11.5	1599.3	0.4	0.9
S-cCNC1300	0.9±0.0	0.6±0.0	0.2±0.0	24.0±0.8	69.4±0.6	11.5	1601.7	0.4	0.9
S-cCNC1400	0.9±0.1	0.6±0.0	0.3±0.0	22.0±0.5	69.0±1.7	11.5	1601.5	0.3	0.7
S-cCNC1500	0.9±0.1	0.7±0.0	0.3±0.0	20.0±0.8	69.1±0.4	13.5	1599.5	0.2	0.5
S-cCNC1600	0.8±0.1	0.6±0.0	0.3±0.0	13.0±0.3	65.7±0.3	11.5	1601.4	0.1	0.4
S-cCNC1800	0.6±0.0	0.6±0.0	0.5±0.0	4.2±0.0	69.7±0.2	11.5	1594.9	0.0	0.1
S-cCNC2000	0.6±0.1	0.6±0.0	0.6±0.0	2.8±0.0	65.2±0.8	11.5	1591.5	0.0	0.1
S-cCNC2200	0.8±0.1	0.7±0.0	0.7±0.0	2.7±0.0	60.2±0.7	13.5	1589.0	0.0	0.0
S-cCNC2400	0.9±0.1	0.9±0.0	0.8±0.0	2.1±0.0	42.1±0.8	17.3	1583.4	0.0	0.0
S-cCNC2500	1.0±0.1	1.0±0.0	0.9±0.1	3.4±0.0	40.2±0.4	19.2	1583.5	0.0	0.0

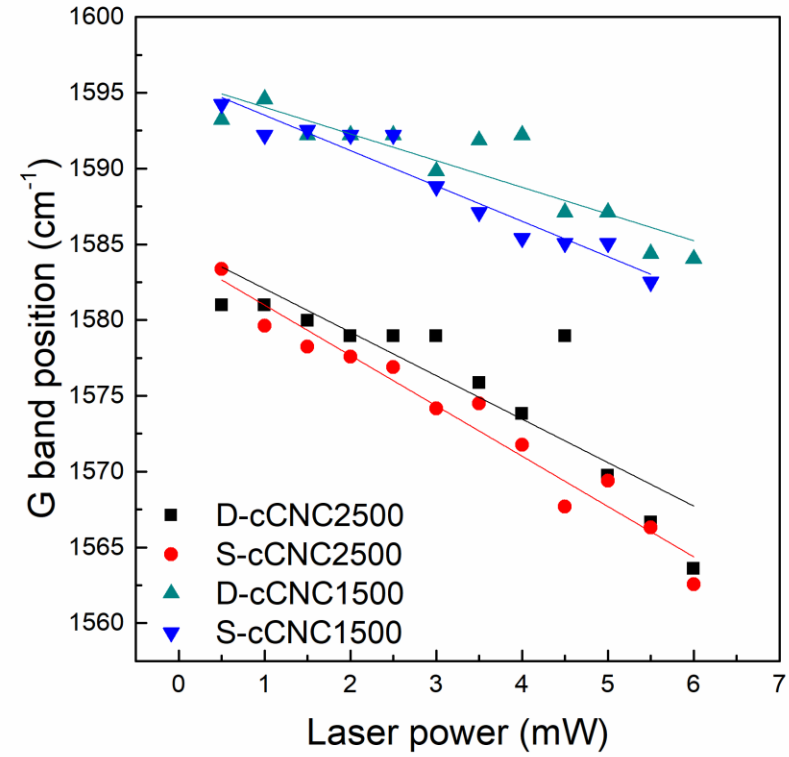

Figure 2.11 G-band position *vs* Laser power of the carbonized CNC.

Table 2.4 Slopes and intercepts of the fitted straight line for the carbonized CNC

		Value	Stdev
D-cCNC1500	Slope	-1.8	0.3
	Intercept	1595.8	1.0
S-cCNC1500	Slope	-2.3	0.2
	Intercept	1595.8	0.7
D-cCNC2500	Slope	-2.9	0.5
	Intercept	1584.9	1.8
S-cCNC2500	Slope	-3.3	0.2
	Intercept	1584.3	0.8

XRD patterns of the D- and S-cCNCs are shown in Figure 2.12. The two XRD peaks neat $2\theta = 26$ and 42° correspond to the (002) and (10) layers of the graphite structure [71, 81]. XRD pattern changes gradually with the increase in temperature, possibly owing to ultrastructural changes in both cCNC samples. At 1000 and 1500 °C, both samples have 17-30° of broad (002) plane. The peak narrows and grows in intensity and peak shifts from 22° to 26° occurs on D-cCNC2000 and S-cCNC2000. It represents structural conversion to graphitic structure and improves in-plane coherence length and atomic ordering. From the peak position of (002) plane, it indicates the inter-layer spacing steadily decrease along the carbonization temperature until it reached 0.34 nm in S-cCNC 2500 and D-cCNC2500.

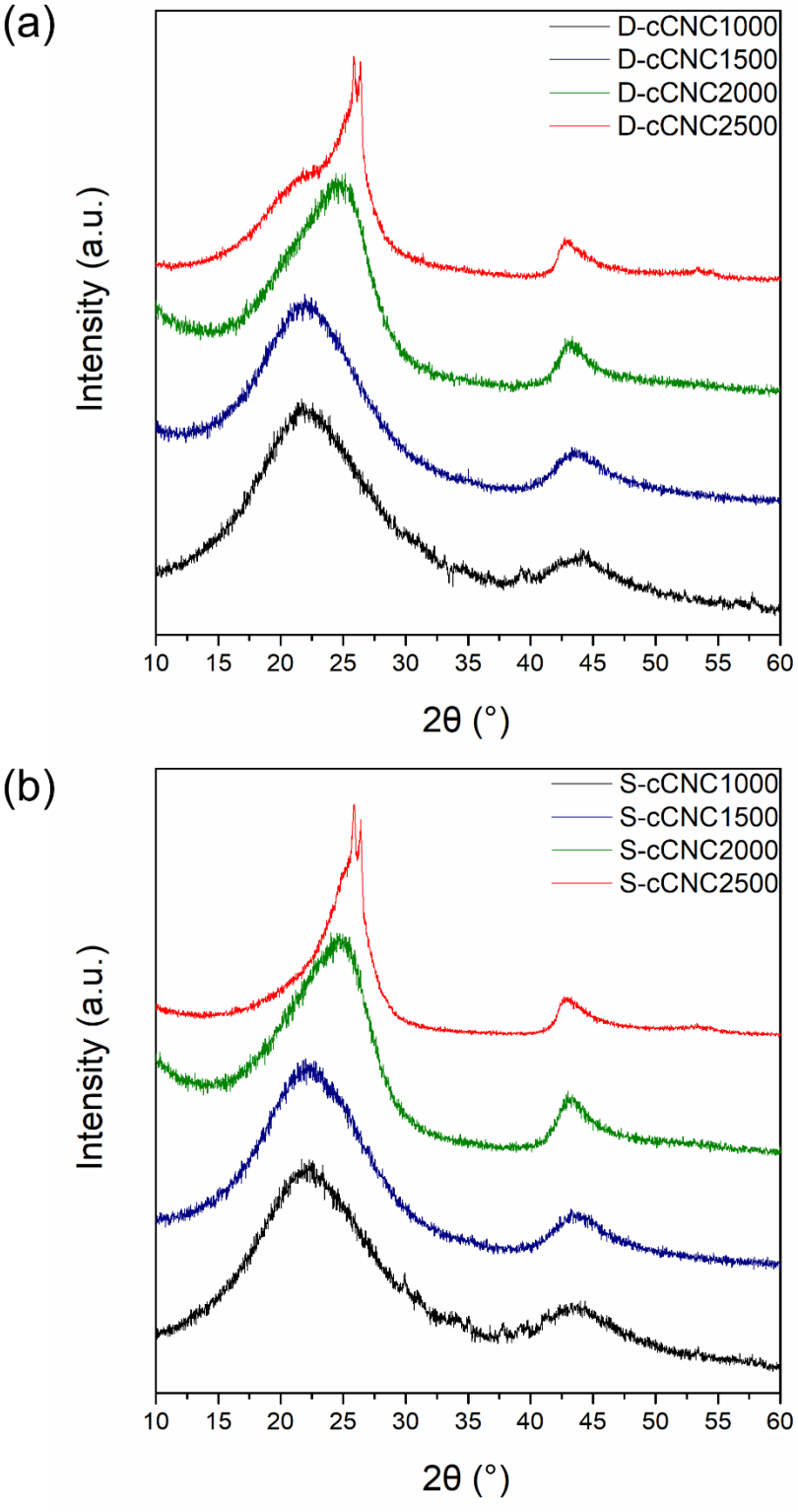

Figure 2.12 WXAD patterns of (a) D-cCNC and (b) S-cCNC.

X-ray photoelectron spectroscopy has frequently been used to characterize the surface chemistry and degree of disorder of the polyaromatic stacks [50-52, 82-86], C_{1s} spectra are selected to find the chemical composition of carbon. The curve fitting of C1s spectra is performed by using a Gaussian-Lorentzian peak shape after performing a background correction by origin-baseline subtraction program. XPS is sensitive to the state of the samples. To evaluate the chemical structure of the surface of cCNCs, peak extraction were processed to the C_{1s} spectra. The extracted peaks appear as in Figure 2.14. by curve fitting. In this case, the peaks correspond to those of aromatic carbon, aliphatic carbon, the C=O peak, or the C-OH peak. The areas of the C_{1s} peak components are calculated and shown in Table 2.7. The $C_{aromatic}/C_{aliphatic}$ ratio of graphite was about 20. The rise of $C_{aromatic}/C_{aliphatic}$ for D- and S-cCNCs samples are due to the formation of some condensed aromatic rings. The component of C3 (C-OH) and C4 (C=O) and C5 (COOH), which contained oxygen atom have a similar value depending on the temperature. Nishiniya et al [52] reported that C3, C4, and C5 were detected until 2,400 ^{o}C carbonization temperature. The composition of C1 represents that sp2 bonding portion increase with increasing carbonization temperature. The composition of C2 suggests that the sp3 bonding decrease with increasing carbonization temperature. Results indicate that the carbon structures are formed above carbonization temperature at 2000 ^{o}C.

Table 2.5 Positions and assignments of C_{1s} peak components

Peak assignments	Binding type	Binding energy (eV)
C1	Graphite/aromatic	284.6
C2	Aliphatic	285.0
C3	C-OH, C-O-C	286.1
C4	C=O	287.6
C5	COOH	290.1
C6	$\pi - \pi^*$	291.2

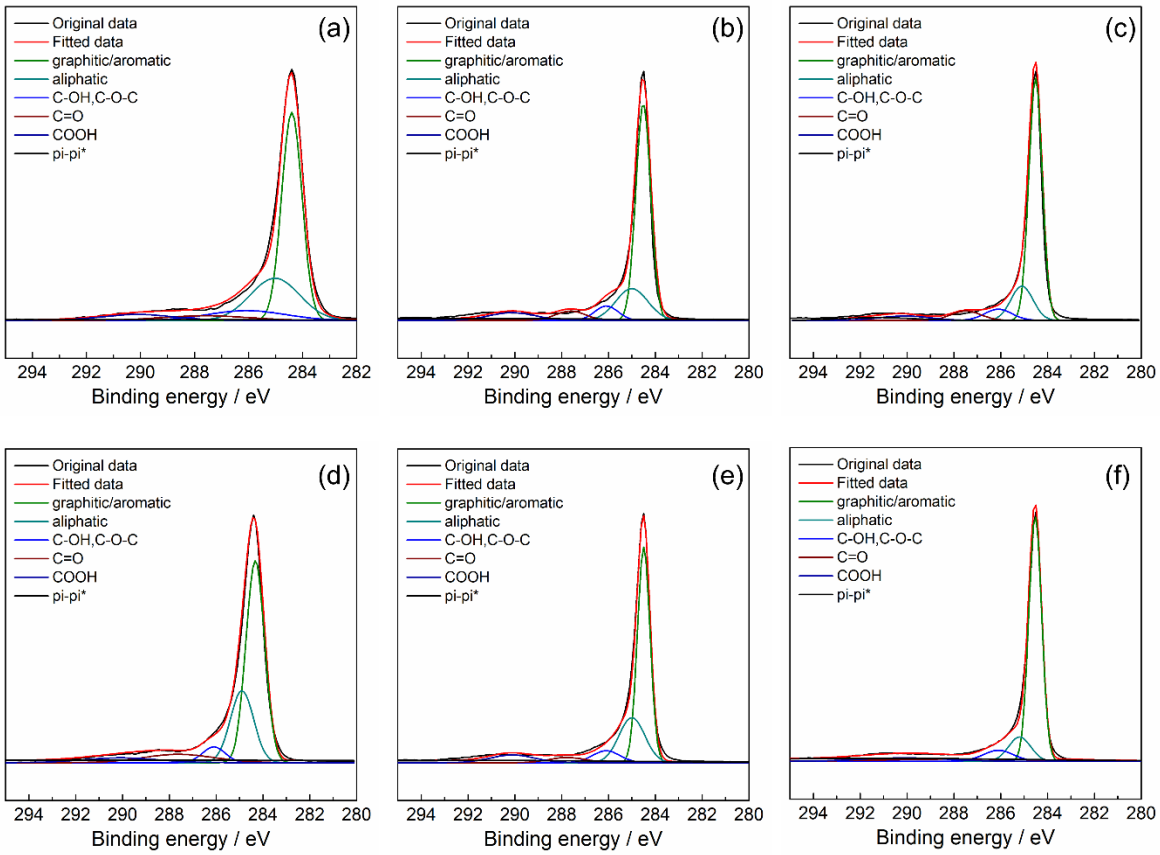

Figure 2.13 Deconvoluted XPS C_{1s} of (a) D-cCNC1500, (b) D-cCNC2000, (c) D-cCNC2500, (d) S-cCNC1500, (e) S-cCNC2000, and (f) S-cCNC2500.

Table 2.6 Positions and assignments of C_{1s} peak components

Samples	C1	C2	C3	C4	C5	C6	C1/C2
D-cCNC1500	52%	26%	9%	5%	5%	3%	2
D-cCNC2000	58%	18%	6%	5%	7%	7%	3.22
D-cCNC2500	65%	15%	6%	6%	5%	4%	4.33
S-cCNC1500	50%	22%	5%	8%	5%	10%	2.27
S-cCNC2000	51%	22%	6%	4%	7%	10%	2.32
S-cCNC2500	58%	10%	6%	6%	5%	14%	5.8

Chapter III Dry-jet wet spinning of PES/CNC composite fibers

3.1 Introduction

3.1.1 Current study for PES/CNC composites

A numerous kind of polymeric materials are available with a wide range of properties. One of the typical categorization method is crystallinity of the polymer. One can have non-crystallizable polymers so called amorphous polymer and the other is crystallizable polymers. In addition, these polymers can also be categorized as a function of their properties. Among them, super engineering plastics are known to have excellent mechanical, chemical, and thermal properties.

Polyetherulfone (PES) is common material for hollow fiber membranes and ultrafiltration (UF) membranes due to good chemical resistance, high mechanical properties and temperature tolerances [87-91]. Ping Qu et al [92] reported PES composite membrane blended with cellulose fibrils. The pure water flux of the composite membrane and mechanical properties were enhanced with the addition of the cellulose fibrils. Parisa et al [93] studied that the presence of CNCs in PES matrix led to a more hydrophilic and became smoother and hydrophilic membranes. In this study, we fabricate the PES/CNC composite fibers by a dry-jet wet spinning method.

3.2 Experimental

3.2.1 Material

Polyethersulfone (PES ultrason E2010 with MW = 18,500 g/mol) is obtained from Basf. CNC purchase from the university of Maine. *N*,*N*-Dimethyl formamide (DMF) and *N*,*N*-Dimethylacetamide (DMAc) from Samchun, Company is used.

3.2.2 Solution Preparation

CNC is dispersed in DMF and DMAc at a concentration of 94 mg/100 mL for 1 week by using bath sonication at room temperature. PES (72g) is dried at 130 °C in vacuum dissolved in DMF (100 mL) at 80 °C. and PES (80g) is dissolved in DMAc (100 mL) at 80 °C. Homogeneous CNC/DMF and CNC/DMAc is added to the PES/DMF and PES/DMAc solution, respectively. The excess amount of solvent is evaporated by vacuum distillation at 100 °C, to obtain the desired solution concentration (80g solid (PES+CNC)/100 mL solvent). The conditions are prepared to yield CNC concentration with respect to the polymer of 1, 2 wt.%. To determine the dispersion of CNC, Optical Microscopy, Scanning Electron Microscopy (FEI, NovaSEM), Transmission Electron Microscopy (JEOL, JEM2900) and Dynamic Light Scattering (Malvern, Nano ZS) are used.

3.2.3 Fiber spinning

From the Table 3.1, control PES fibers are spun from DMF at 3.5 m/min using 150 μm diameter with 8 holes spinneret at 60 °C into the water bath maintained at 10°C. The air gap between the spinneret and the water bath is about 3 mm. The as-spun fibers are taken up at 10 m/min and are kept immersed in water bath for 1 day, to remove the solvent. As a result, the draw ratio of as-spun fibers are 2.8. The as-spun fibers are further maximum drawn at each temperature from 70 to 160 °C and vacuum drying at 100 °C for 1 days. The total draw ratio determined by multiplying spin draw ratio, with post draw ratio, is as high as 6.4 listed in Table 3.1. Control PES fibers are spun from DMAc at 3.5 m/min using 150 μm diameter with 8 holes spinneret at 60 °C into a water bath maintained at 10 °C. The air gap between the spinneret and the water bath is about 3 mm. The as-spun fibers are taken up at 7 m/min and 11.2 m/min and kept immersed in water bath for 1 day, to remove the DMAc solvent. As a result, the as-spun fibers are 2 and 3.2, respectively. The as-spun fibers are further drawn and vacuum drying at 100 °C for 1 day. The total draw ratio is determined by multiplying spin draw ratio with post draw ratio.

3.2.4 Fiber characterization

Fiber tensile fracture surface is observed on the gold coated sample by scanning electron microscopy (FEI, Nova Nano SEM). Using the FAVIMAT+ (TexTecnno, GmbH, Germany) for single filament tensile testing and linear density (fiber diameter) are measured by vibroscope, which relates the resonance frequency of a single filament to its mass per unit length, measured in units of tex (1 tex = 1 g/1000 m). Pre-tension is 1.3 cN / tex and the gauge length is 1 inch for the typical tensile testing condition for linear density measurement. For each sample, 50 filaments are tested.

3.3 Result and Discussion

3.3.1 Dispersion study of CNC in DMAc and DMF solution

HR-TEM data (Figure 3.1) shows CNC with 5-20 nm in diameter and 50-200 nm. Figure 3.1 (b) inset image indicate the high crystalline phase of CNC. To disperse CNC, both horn-type sonication and bath-type sonication are used. Due to hydrogen bonding and van der Waals interaction of CNC, dispersion of CNC is one of the critical parts. Therefore, it is prerequisite to optimize the dispersion conditions of CNC in a given organic solvent. OM, SEM, and DLS are used to determine the optimum condition of CNC dispersion. Dispersion of CNC state with increasing sonication time is shown in Figure 3.2. With increasing sonication time, the particle size of CNC becomes smaller. We observed the CNC dispersion by using SEM. Figure 3.3 indicates one can see that the CNC sample has spherical particle shape after 5 min sonication. After 150 min sonication, however, the globular shape CNC particles are opened up and eventually exhibit nano-fibrillar shape. Figures 3.4 (a-b) exhibit the DLS

spectra of CNC/DMF and solution as a function of sonication time. Based on the theory of Stokes-Einstein relationship, and Kirkwood and Riseman results [40] ($D_h = L/\ln(L/d)$), the estimated hydrodynamic diameter (D_h) of the CNC from U. of Maine ($d \approx 5$ nm, $L \approx$ 150-200 nm) is supposed to be in the range of 44 – 54 nm by assuming the rod shape particle**.** Figure 3.4(a) is showing the relationship between size distribution of the dispersed CNC particle and hydrodynamic diameter of them. The size distribution becomes narrower and the hydrodynamic diameter gets smaller. Figure 3.4(b) shows the variation of hydrodynamic diameter becomes smaller rapidly in the beginning of sonication and got saturated at above 3 hours of sonication time. One can calculate the theoretical hydrodynamic diameter based on the manufacturer-provided CNC dimension, which is in the range of 44-54 nm. One can see that, Upon using horn-type sonication, 150 min of sonication time was required to obtain highly dispersed individual CNC. The well dispersed CNC particles exhibit the average hydrodynamic diameter of about 46 nm. Although horn-type sonication is very powerful tool for CNC dispersion, they have titanium-tip erosion problem that is critical to process nanocomposites. Therefore, we have tried to use bath-type sonication, where the dispersion is not directly exposed to the sonication. As we did the dispersion experiment using horn-type sonication, we have conducted similar experiment by using bath-type sonication. Since the dispersion power of bath-type sonication is much weaker than that of the horn-type sonication, it showed the saturation time at around 30 hours. Figure 3.4 (c) and (d) shows the DLS data by using bath-type sonication. 48 hours of sonication time is required to disperse the CNC individually. Due to the impurity issue generated by the horn-type sonication, we have conducted the bath-type sonication to disperse CNC for nanocomposite manufacturing.

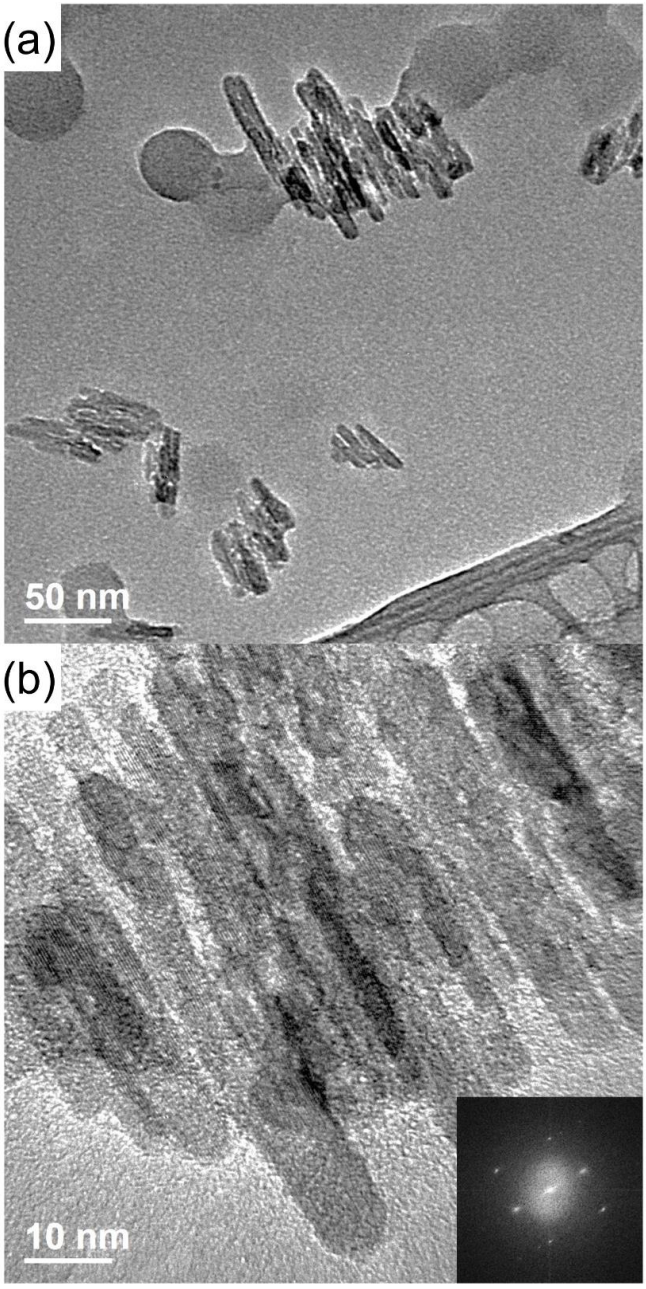

Figure 3.1 HR-TEM images of (a) pristine CNC and (b) high magnification of pristine CNC. The inset figure represents the diffraction pattern of corresponding sample.

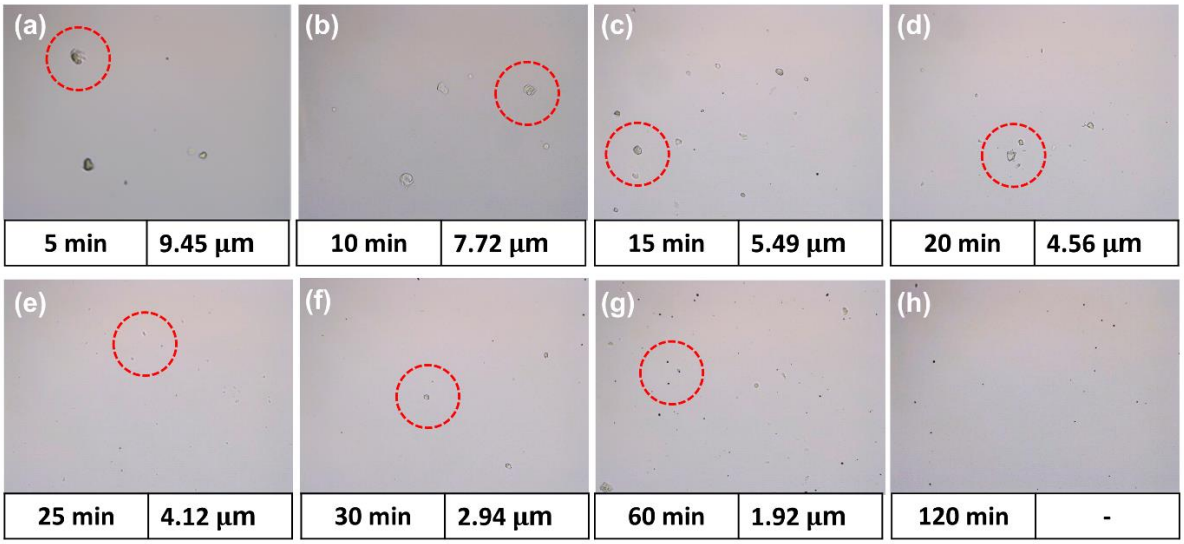

Figure 3.2 Optical Microscopy images of dispersed CNC in DMF (94 mg/100 ml) with various sonication time.

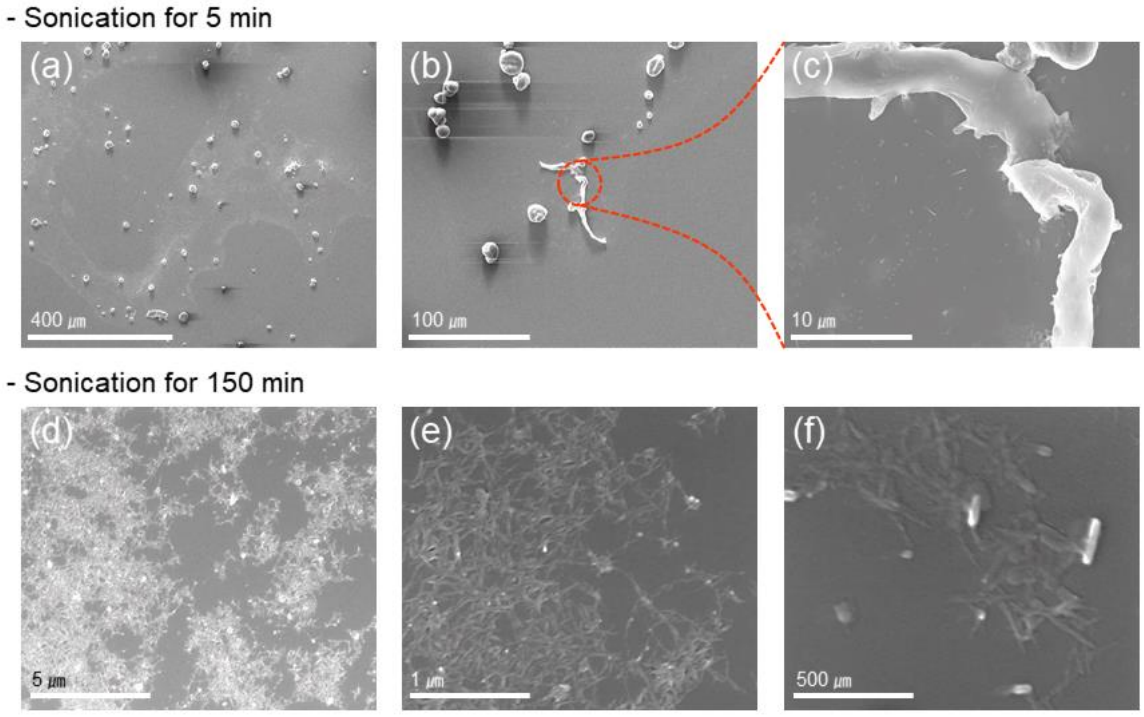

Figure 3.3 FE-SEM images of dispersed CNC; (a), (b) and (c) sonication for 5 min in DMF (94 ml/dl); (d), (e) and (f) sonication for 150 min in DMF (94 ml/dl).

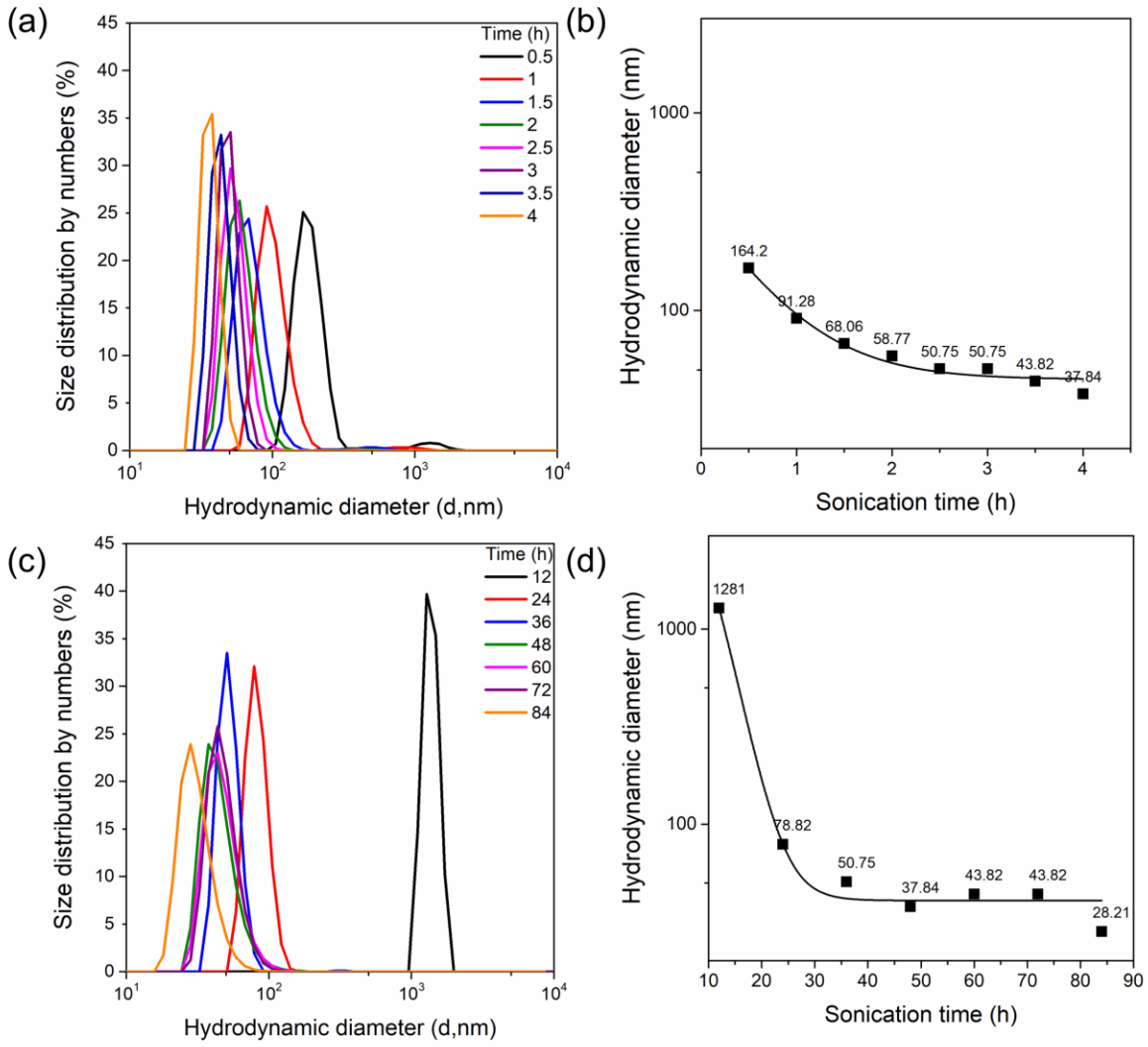

Figure 3.4 Dynamic Light scattering data by using horn-type sonication with 0.1 wt.% concentration of CNC in DMF solution. (a) Size distribution of CNC with different sonication time and (b) Hydrodynamic radius of CNC in DMF with different sonication time. Dynamic Light scattering data by using bath-type sonication with 0.1 wt.% concentration of CNC in DMAc solution. (c) Size distribution of CNC with different sonication time and (d) Hydrodynamic radius of with different sonication time.

3.3.2 Tensile properties of PES and PES/CNC composite fibers

Tensile properties of Control PES fibers are listed in Table 3.1. The PES fibers spun from DMF solvent (72 g/dl). From the Figure 3.5, with increasing post-spin draw ratio, PES fibers become stiffer and stronger. PES 1-1* and PES 1-1-5 fibers have the diameter of 47.3 and 38.5 μm, respectively. Drawing at around 110 °C (PES 1-1-3) appears to be the optimum condition for the balance between strength and modulus (high toughness). For PES 1-1-3 sample, the tensile strength and modulus are 128.6 MPa and 2.8 GPa, respectively, which is about 16% and 29% higher than the as-spun PES fibers (1-1*). Figure 3.5 indicates the stress-strain curve of control PES fibers spun from DMF solvent. The Result indicates that the tensile strength increases with increasing draw ratio. It also indicates that the tensile strength and toughness are highest for PES 1-1-3.

However, from the figure 3.6, the PES/DMF solutions exhibit gelation behavior with storing below about 50 °C. As shown in variation of the storage modulus (G') in the temperature cycle test, the PES solution undergoes gelation by cooling and holding at 10 °C and gel recover to the solution state upon heating above the critical temperature (T_C) of 48.6 °C. The spinning temperature is maintained at 60 °C to prevent gelation. Due to gelation issues, solvent is changed from DMF to DMAc. Moreover, the PES fiber spun from DMF solvent (72 g/100 ml) have lots of porous structure on fracture surface (Figure 3.7). To reduce the porous structure on the PES fracture surface, the concentration of the solution increases to 80g PES/100 ml DMAc during the spinning.

Tensile properties of PES fibers spun from DMAc solvent is given in Table 3.2. The diameter of Control PES fibers decrease with increasing draw ratio. Strain to failure and Toughness of PES fibers increase with increasing draw ratio. In case of PES 2-1-3 samples, post-drawing is performed at 100 °C. The modulus and strength of PES 2-1-3 increase by 143% and 235%, respectively, compared to the as-spun fibers. Due to increasing PES solid concentration, the tensile properties of PES 2-1 samples are higher than PES1-1 samples. Figure 3.7 represents the strain-stress curve of PES fibers spun from DMAc solvent. Likewise, compare with PES 2-1* as-spun fiber, the samples with post-drawing have high tensile modulus and strength.

Table 3.1 Tensile properties of PES fibers spun from DMF solvent.

		Drawing Temp (°C)	Draw ratio	Diameter (um)	Tensile Strength (MPa)	Tensile Modulus (GPa)	Strain to failure (%)	Toughness (J/g)
PES	1-1*	As-spun: 2.8		47.3±1.4	78.6±3.8	1.9±0.6	94.8±5.2	41.0±6.3
PES	1-1-1	70	4.1	41.6±1.0	108.5±6.5	2.6±0.2	55.7±9.1	39.3±7.0
PES	1-1-2	90	4.1	42.4±0.9	104.0±3.7	2.4±0.2	70.8±5.4	47.9±2.9
PES	1-1-3	110	5.1	38.5±1.1	128.6±8.7	2.8±0.1	39.0±9.7	38.4±1.0
PES	1-1-4	130	5.6	36.3±1.4	116.5±7.3	2.7±0.1	16.1±11.0	36.7±1.6
PES	1-1-5	140	6.4	33.2±0.9	122.8±6.7	2.7±0.2	7.1±0.4	4.5±0.46

*as-spun fiber

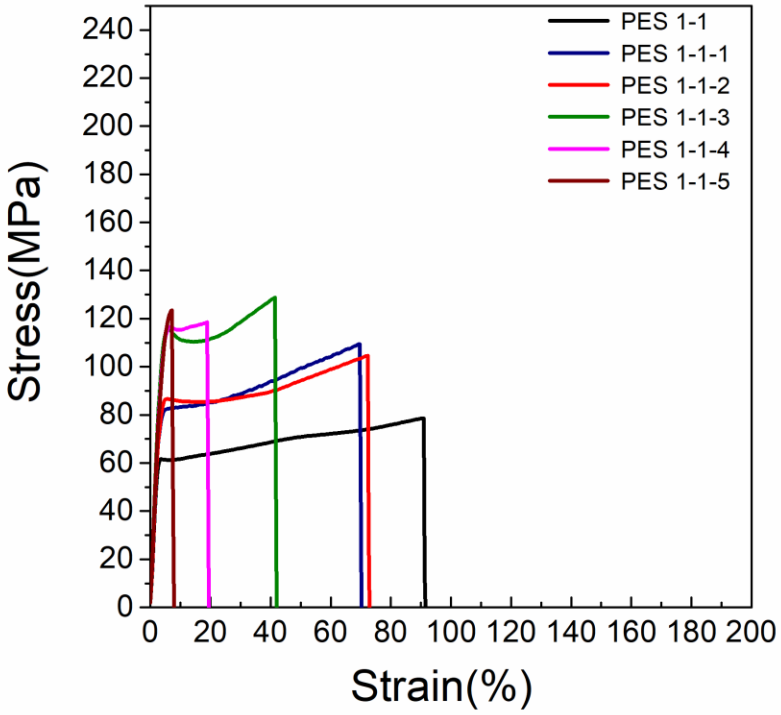

Figure 3.5 Stress-strain curve of PES fibers spun from DMF solvent.

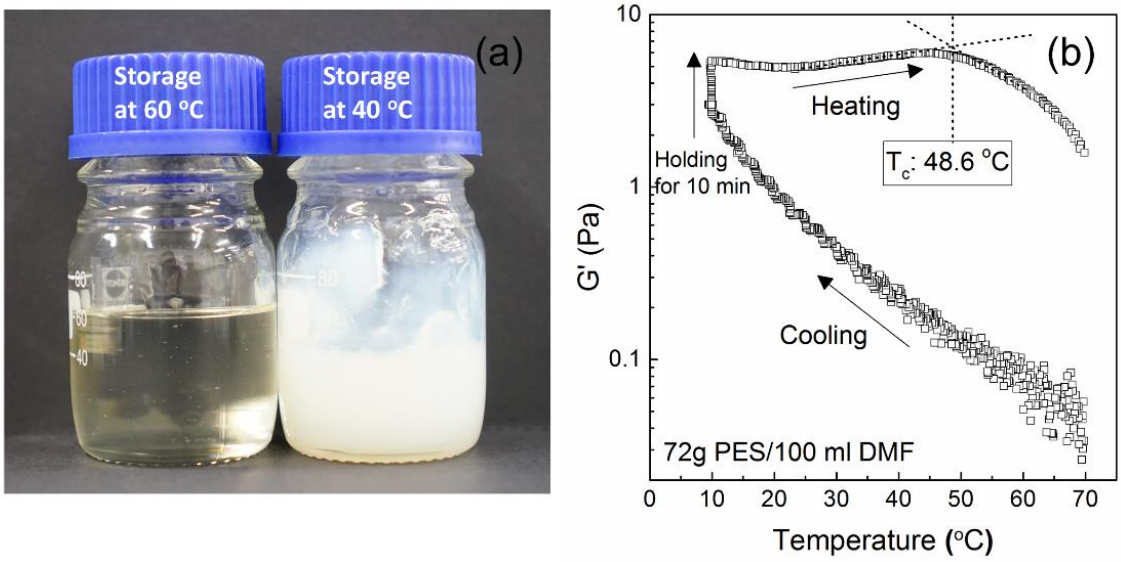

Figure 3.6 (a) Photographs of PES/DMF solutions; left images indicates PES/DMF solution stored at 60 °C and right images shows PES/DMF solution stored at 40 °C. (b) Rheological characteristics of phase stability of PES/DMF solution.

Table 3.2 Tensile properties of PES fibers spun from DMAc solvent

		Drawing Temp (°C)	Draw ratio	Diameter (um)	Tensile Strength (MPa)	Tensile Modulus (GPa)	Strain to failure (%)	Toughness (J/g)
PES	2-1*	As-spun: 2.0		46.3±3.4	88.9±15.8	2.6±0.4	4.6±0.9	2.0±0.7
PES	2-1-1	80	4.1	47.8±1.3	157.3±8.3	3.1±0.1	54.5±5.0	50.1±5.5
PES	2-1-2	90	4.1	44.7±2.2	174.3±16.3	3.4±0.2	42.8±7.7	44.6±7.3
PES	2-1-3	100	5.1	41.2±1.6	207.5±12.1	3.9±0.1	35.7±5.9	44.2±6.6
PES	2-1-4	110	5.6	38.0±2.0	180.4±11.5	3.8±0.2	13.9±3.4	14.8±4.3
PES	2-1-5	120	6.4	38.8±2.4	148.6±17.5	3.4±0.2	18.9±12.3	18.2±13.7

*as-spun fiber

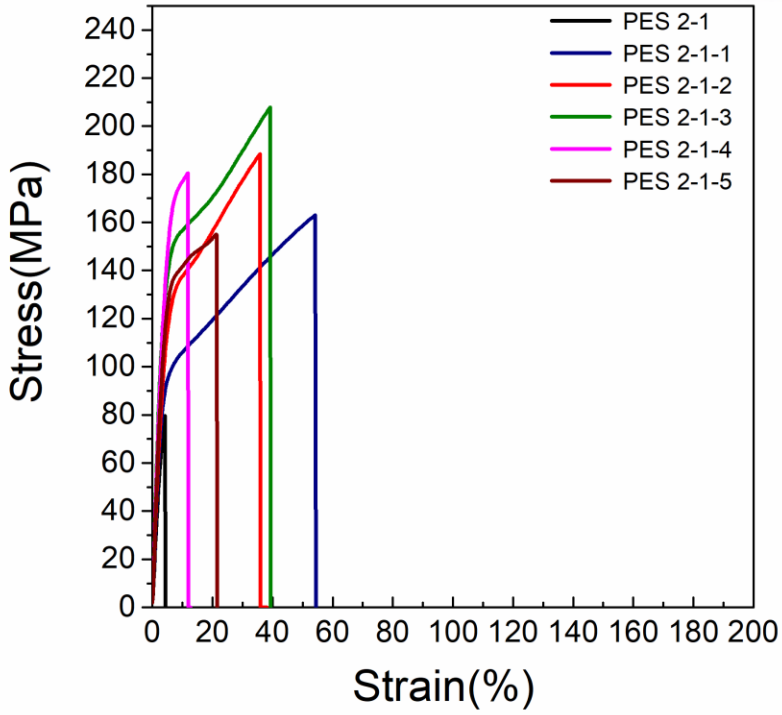

Figure 3.7 Stress-strain curves of PES fibers spun from DMAc.

Tensile properties of PES fibers spun from DMAc solvent with draw ratio 3.2 are listed in Table 3.3. From the Table 3.1 and 3.2, we obtain fibers with maximum tensile properties on drawing temperature at 100-110 °C. Therefore, we proceed post-drawing at 100 °C. For PES 3.1-2 fibers, the modulus and strength are increased by 73% and 278%, respectively compared with the as-spun fibers. From the Table 3.2 and Table 3.3, as-spun 3.2 fibers (PES 3-1*) have higher tensile properties. Tensile properties of PES_CNC1 composite fibers are given in Table 3.4. For PES/CNC1 composite fibers with Draw ratio 2, there is no difference between PES control fiber and PES/CNC1 composite fibers. Compare with the maximum achievable draw ratio with CNC1 1-1-3 samples and PES 2-1-5 samples, the tensile strength and toughness of CNC1 1-1-3 samples are slightly higher than PES 2-1-5 samples. However, the modulus of CNC1 1-1-3 samples is slightly lower than PES 2-1-5 samples. For PES/CNC1 composite fibers with Draw ratio 3.2, tensile properties of PES/CNC1 with as-spun draw ratio 3.2 composites fiber have higher tensile properties than PES and PES/CNC1 with as-spun draw ratio 2.0. Compare with PES 3-1-1 and PES/CNC1 2-1-1 samples, tensile strength and modulus of PES/CNC1 2-1-1- samples increase by 20% and 30%, respectively. Moreover, PES/CNC1 fibers with 3.2 as-spun fiber draw ratio show higher tensile properties compared to PES/CNC1 fibers with 2.0 as-spun fiber draw ratio.

With the incorporation of CNC suggests a tendency for increasing tensile properties. Crystallinity, orientation and crystal size increase with increasing draw ratio. Composite fibers exhibited slightly higher tensile properties when compared to the control fiber of the sample draw ratio (DR 4.8 and 8).

Figure 3.11 indicates the tensile properties of PES/CNC1 composite fibers. Both graphs show that tensile properties increase with increasing draw ratio. For PES/CNC2 composite fibers, the tensile properties all samples lower than the PES control fibers from the Table 3.5. In case of PES/CNC2 composite fibers, it can be confirmed that CNC does not effectively as a reinforcing agent and fillers. PES/CNC 2 composite fibers with as-spun draw ratio 2.0, the CNC2 1-1-3 has the maximum tensile strength of 163 MPa and modulus of 3.7 GPa. PES fibers with as-spun draw has the maximum tensile strength of 207.5 MPa and modulus of 3.9 GPa. PES/CNC2 composite fiber has lower tensile properties than PES control fibers. Moreover, PES/CNC 2 composite fibers with as-spun draw ratio 3.2, it has the maximum tensile strength of 207.8 and modulus of 3.9 (CNC2 2-1-3).

Table 3.3 Tensile properties of PES fibers spun from DMAc solvent with draw ratio 3.2

		Drawing Temp (°C)	Draw ratio	Diameter (um)	Tensile Strength (MPa)	Tensile Modulus (GPa)	Strain to failure (%)	Toughness (J/g)
PES	3-1*	As-spun: 3.2		48.8±0.6	82.8±1.5	2.7±0.1	175.4±5.8	96.1±3.5
PES	3-1-1	100	4.8	41.9±0.8	115.8±3.6	3.0±0.1	115.9±4.3	85.2±4.5
PES	3-1-2	100	8.0	31.0±1.1	230.1±10.1	4.0±0.1	27.0±3.6	36.4±4.9

*as-spun fiber

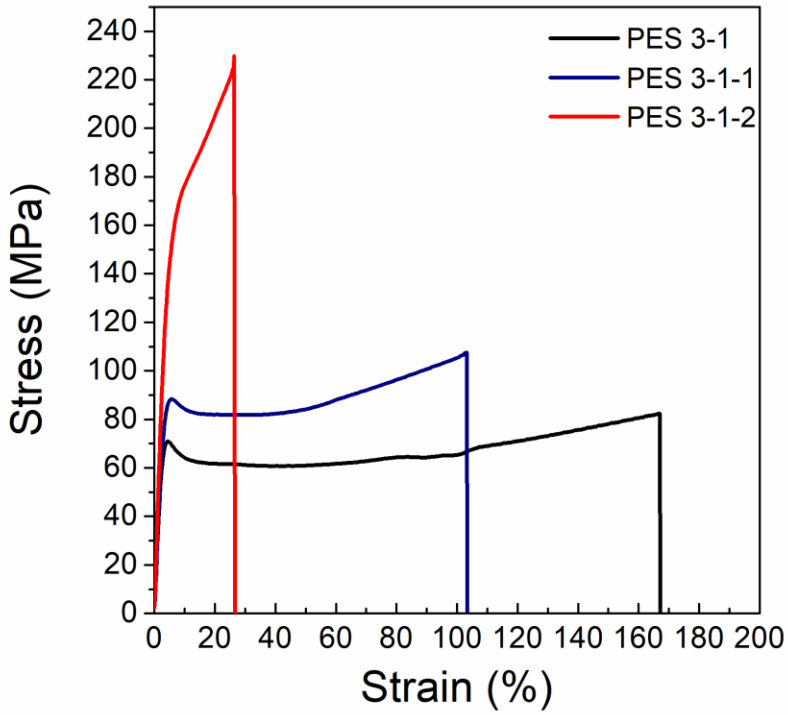

Figure 3.8 Stress-strain curve of PES fibers spun from DMAc solvent.

Table 3.4 Tensile properties of PES/CNC1 spun from DMAc solvent

		Drawing Temp. (°C)	Draw ratio	Diameter (um)	Tensile Strength (MPa)	Tensile Modulus (GPa)	Strain to failure (%)	Toughness (J/g)
CNC1	1-1	As-spun: 2.0		47.2±1.1	76.1±8.4	2.8±0.1	153.6±12.7	75.3±8.4
CNC1	1-1-1	100	3.0	50.4±1.7	135.9±8.4	3.4±0.1	107.0±5.8	90.5±7.2
CNC1	2-1-2	100	4.0	43.7±0.8	187.5±8.7	4.0±0.1	61.1±4.2	69.7±6.8
CNC1	1-1-3	100	5.0	40.7±0.6	212.8±8.2	3.7±0.1	42.6±4.0	64.5±5.2
PES	1-1-5	100	5.0	41.2±1.6	207.5±12.1	3.9±0.1	35.7±5.9	44.2±6.6
CNC1	2-1	As-spun: 3.2		46.6±0.6	88.7±5.3	2.8±0.4	178.8±23.4	96.3±15.4
CNC1	2-1-1	100	4.8	41.8±0.8	134.2±5.0	3.1±0.1	119.8±6.9	96.2±6.0
CNC1	2-1-2	100	6.4	35.4±0.7	191.1±10.9	4.0±0.1	59.6±6.0	70.2±8.4
CNC1	2-1-3	100	8.0	31.9±0.7	240.4±8.4	4.7±0.1	34.3±5.8	51.8±10.2
PES	3-1-2	100	8.0	31.0±1.1	230.1±10.1	4.0±0.1	27.0±3.6	36.4±4.9

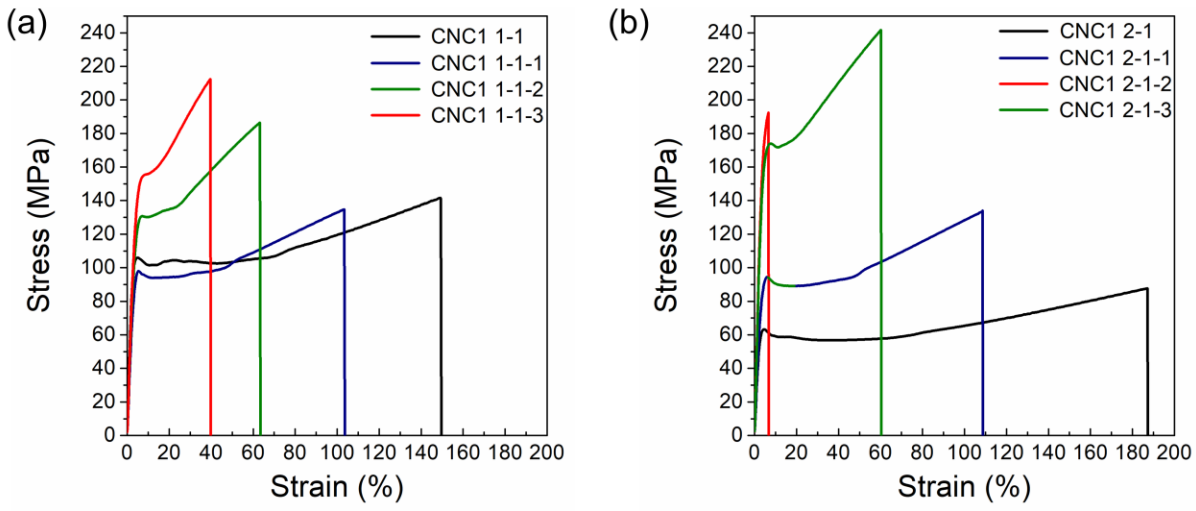

Figure 3.9 Tensile properties of PES_CNC1 composites fibers spun from DMAc; (a) Stress-strain curve of PES_CNC1 with as -spun draw ratio 2.0. (b) Stress-strain curve of PES_CNC1 with as -spun draw ratio 3.2.

Table 3.5 Tensile properties of PES/CNC2 spun from DMAc solvent

		Drawing Temp (°C)	Draw ratio	Diameter (um)	Tensile Strength (MPa)	Tensile Modulus (GPa)	Strain to failure (%)	Toughness (J/g)
CNC2	1-1	As-spun: 2.0		57.0±1.2	76.1±8.4	2.7±0.1	142.6±15.4	66.5±8.7
CNC2	1-1-1	100	3.0	44.4±1.0	125.2±5.3	3.4±0.1	76.7±9.9	61.6±7.9
CNC2	1-1-2	100	4.0	42.1±0.7	153.5±5.3	3.5±0.1	56.2±5.4	53.6±5.8
CNC2	1-1-3	100	4.2	34.9±0.9	163.2±7.1	3.7±0.1	42.6±4.0	54.3±5.4
PES	2-1-3	100	5.0	41.2±1.6	207.5±12.1	3.9±0.1	35.7±5.9	44.2±6.6
CNC1	1-1-3	100	5.0	40.7±0.6	212.8±8.2	3.7±0.4	42.6±4.0	64.5±5.2
CNC2	2-1	As-spun: 3.2		46.0±1.4	73.3±6.4	2.7±0.1	143.7±28	67.6±16.6
CNC2	2-1-1	100	4.8	38.8±0.7	112.2±6.8	3.1±0.1	67.0±10.7	91.6±12.2
CNC2	2-1-2	100	6.4	33.7±0.5	156.1±5.9	3.7±0.1	55.4±9.5	54.0±10.2
CNC2	2-1-3	100	8.0	30.6±1.1	206.8±8.7	3.9±0.1	38.7±3.3	48.3±4.6
PES	3-1-2	100	8.0	31.0±1.1	230.1±10.1	4.0±0.1	27.0±3.6	36.4±4.9
CNC1	2-1-3	100	8.0	31.9±0.7	240.4±8.4	4.7±0.1	34.3±5.8	51.8±10.2

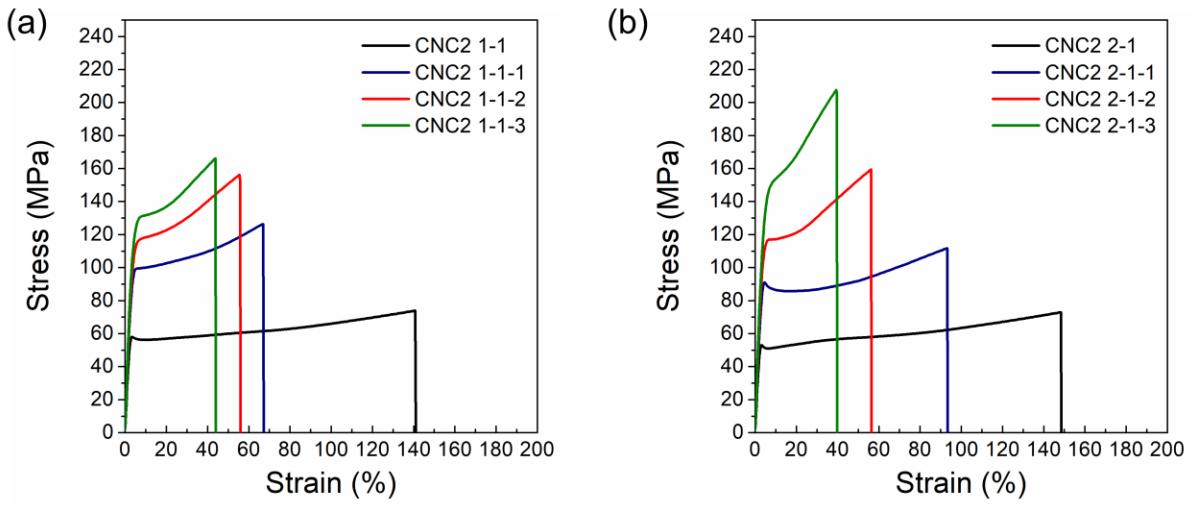

Figure 3.10 Tensile properties of PES_CNC2 composites fibers spun from DMAc; (a) Stress-strain curve of PES_CNC2 with as -spun draw ratio 2.0. (b) Stress-strain curve of PES_CNC2 with as -spun draw ratio 3.2.

Table 3.6 Comparison of tensile properties of PES/CNC composite fibers

	Draw ratio	Diameter (um)	Tensile Strength (MPa)	Tensile Modulus (GPa)	Strain to failure (%)	Toughness (J/g)
PES_CNC0	8.0	31.0±1.1	230.1±10.1	4.0±0.1	27.0±3.6	36.4±4.9
PES_CNC1	8.0	31.9±0.7	240.4±18.4	4.7±0.1	34.3±5.8	51.8±10.2
PES_CNC2	8.0	30.6±0.6	206.8±8.7	3.9±0.1	38.7±3.3	48.3±4.6

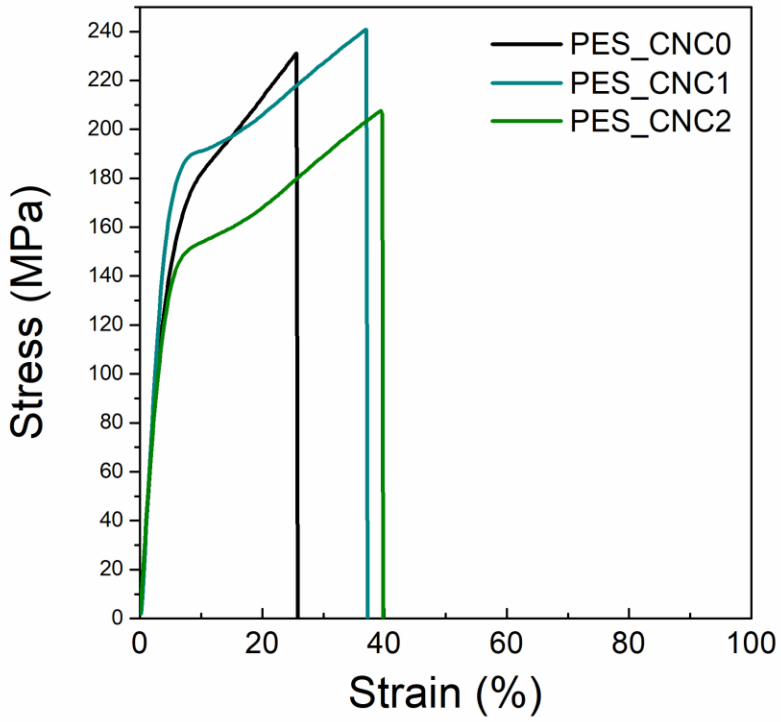

Figure 3.11 Tensile properties of PES_CNC2 composites fibers spun from DMAc; (a) Stress-strain curve of PES_CNC2 with as -spun draw ratio 2.0. (b) Stress-strain curve of PES_CNC2 with as -spun draw ratio 3.2

Mechanical properties of the various structural parameter for the control PES fibers and composite fibers are listed in Table 3.6. PES/CNC1 composite fibers exhibit improved mechanical properties over the control PES fibers. With the addition of 1 wt.% of CNC, modulus and strength increase 17% and 4% respectively. Increase in modulus and strength, toughness is the highest in PES CNC1 composites fibers. This suggests a change in the PES matrix with the incorporation of CNC due to hydrogen bonding. However, in case of PES/CNC2 composite fibers, the tensile modulus and strength are decreased compare with PES control fibers and PES/CNC1 composite fibers.

Addition of CNC increases with strain to failure and toughness, while other conventional fillers and reinforcements improve modulus and strength at the expense of strain to failure and toughness. In this study improved the strain to failure, including to 142% improvement in fiber toughness as measured from the area under the stress-strain curve.

3.3.3 Fiber Morphology of PES and PES/CNC composite fibers

The tensile fracture fiber surfaces and surface morphology of PES fibers spun from DMF solvent are shown in figure 3.12 and 3.13. As the draw ratio increases, the diameter of PES control fibers decreases. In addition, SEM image of fracture surface also confirms that the diameter of PES control fibers decrease. However, there are still lots of porous structure on the surface of PES control fibers.

Figure 3.10 indicates surface fracture images of PES fibers spun from DMAc solution. Compare with Figure 3.7 and Figure 3.9, they can be shown the pore site of fracture surface decreased. From the figure 3.14, tensile fracture surfaces do not reveal fibrillar structure in all samples. Fibril ends are not observed in PES/CNC composite fibers. Figure 3.14 (c) and (f) indicate PES/CNC2 composite fibers. Oriented structures are observed in PES/CNC2 composite fibers. It should be noted that fibrillar structure is observed only in the PES/CNC2 fibers. The highly oriented structure seems to be ascribed to a slow relaxation behavior of pes chains upon fiber drawing due to steric hinderance and interaction with CNC molecules.

For PES fibers, CNC does not have a significant effect on the tensile properties of PES fibers due to the pore structure of PES rather than the effect of reinforcement of CNC.

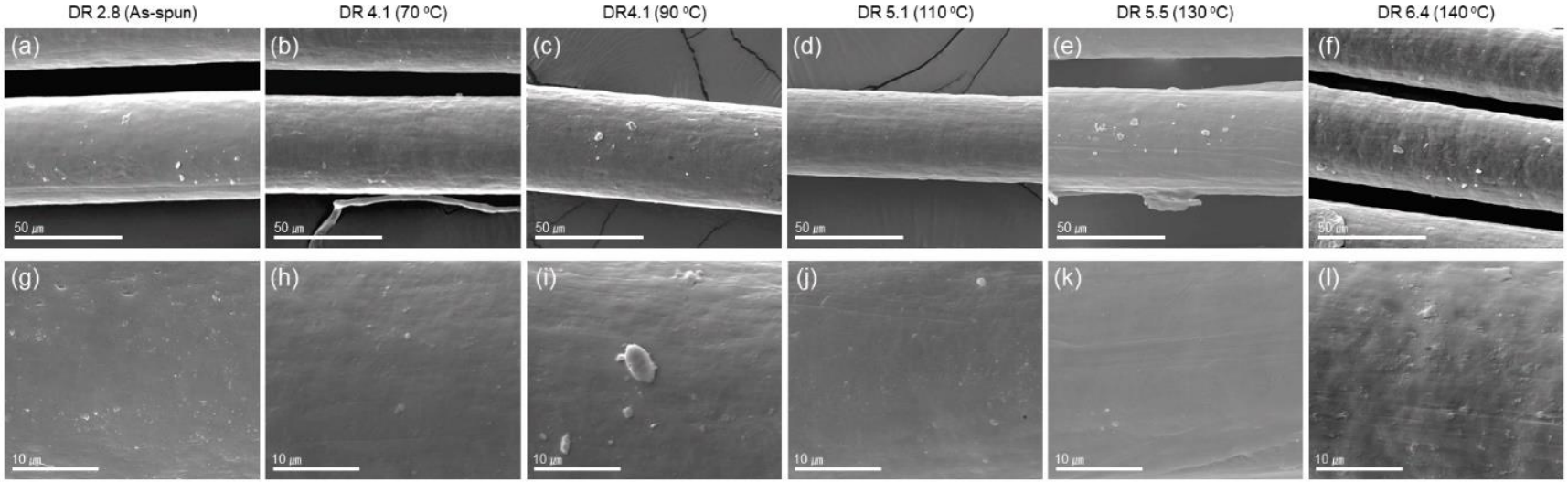

Figure 3.12 Surface morphology of PES fibers spun from DMF solvent.

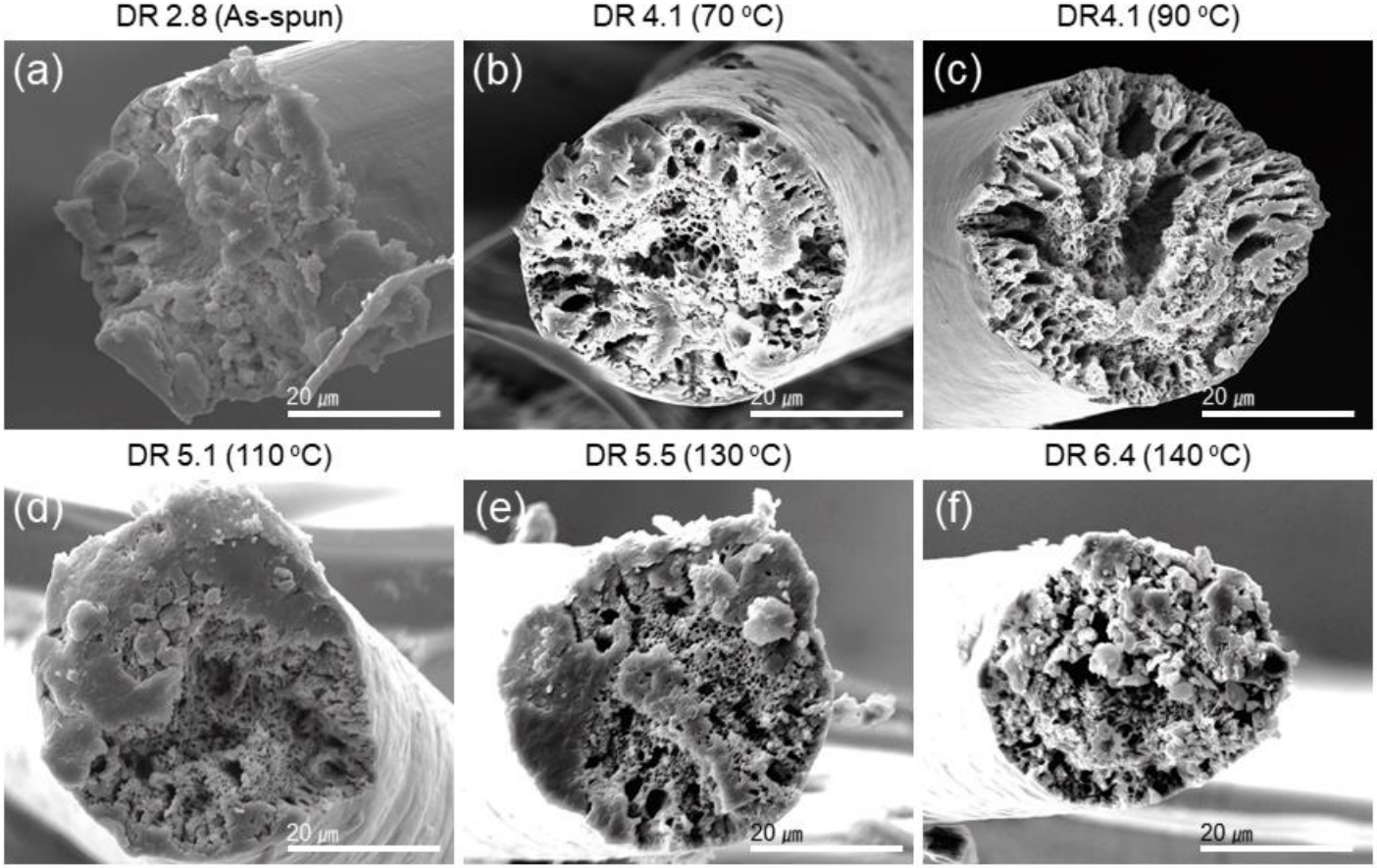

Figure 3.13 Fracture surface morphology of PES fibers depending on draw ratio.

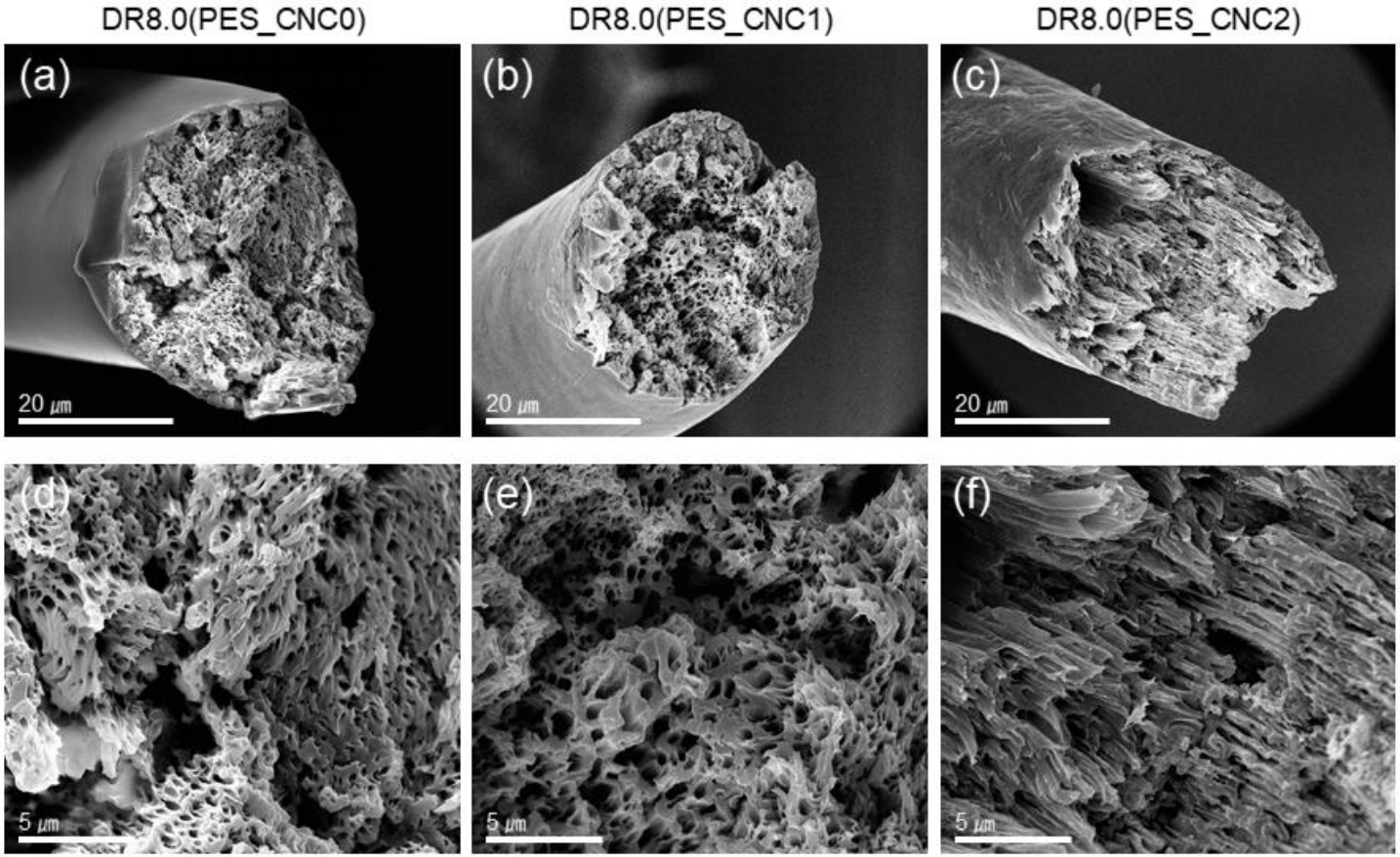

Figure 3.14 Fracture surface morphology of PES_CNC fibers. (a), (d) PES_CNC0 fibers, (b), (e) PES_CNC1 fibers and (c), (f) PES_CNC2 fibers.

Reference

[1] M.A.S.A. Samir, F. Alloin, A. Dufresne, Review of recent research into cellulosic whiskers, their properties and their application in nanocomposite field, Biomacromolecules 6(2) (2005) 612-626.

[2] T.J. Mcdonough, Wood Chemistry - Fundamentals and Applications - Sjostrom,E, J Am Chem Soc 105(13) (1983) 4503-4503.

[3] Y. Habibi, L.A. Lucia, O.J. Rojas, Cellulose Nanocrystals: Chemistry, Self-Assembly, and Applications, Chem Rev 110(6) (2010) 3479-3500.

[4] A. Sturcova, I. His, D.C. Apperley, J. Sugiyama, M.C. Jarvis, Structural details of crystalline cellulose from higher plants, Biomacromolecules 5(4) (2004) 1333-1339.

[5] Y. Nishiyama, J. Sugiyama, H. Chanzy, P. Langan, Crystal structure and hydrogen bonding system in cellulose 1(alpha), from synchrotron X-ray and neutron fiber diffraction, J Am Chem Soc 125(47) (2003) 14300-14306.

[6] S.J. Eichhorn, A. Dufresne, M. Aranguren, N.E. Marcovich, J.R. Capadona, S.J. Rowan, C. Weder, W. Thielemans, M. Roman, S. Renneckar, W. Gindl, S. Veigel, J. Keckes, H. Yano, K. Abe, M. Nogi, A.N. Nakagaito, A. Mangalam, J. Simonsen, A.S. Benight, A. Bismarck, L.A. Berglund, T. Peijs, Review: current international research into cellulose nanofibres and nanocomposites, J Mater Sci 45(1) (2010) 1-33.

[7] G. Siqueira, J. Bras, A. Dufresne, Cellulosic Bionanocomposites: A Review of Preparation, Properties and Applications, Polymers-Basel 2(4) (2010) 728-765.

[8] I. Siro, D. Plackett, Microfibrillated cellulose and new nanocomposite materials: a review, Cellulose 17(3) (2010) 459-494.

[9] D. Klemm, F. Kramer, S. Moritz, T. Lindstrom, M. Ankerfors, D. Gray, A. Dorris, Nanocelluloses: A New Family of Nature-Based Materials, Angew Chem Int Edit 50(24) (2011) 5438-5466.

[10] S. Pirani, R. Hashaikeh, Nanocrystalline cellulose extraction process and utilization of the byproduct for biofuels production, Carbohyd Polym 93(1) (2013) 357-363.

[11] A. Chakraborty, M. Sain, M. Kortschot, Cellulose microfibrils: A novel method of preparation using high shear refining and cryocrushing, Holzforschung 59(1) (2005) 102-107.

[12] B. Wang, M. Sain, Dispersion of soybean stock-based nanofiber in a plastic matrix, Polym Int 56(4) (2007) 538-546.

[13] S. Iwamoto, A.N. Nakagaito, H. Yano, M. Nogi, Optically transparent composites reinforced with plant fiber-based nanofibers, Appl Phys a-Mater 81(6) (2005) Cp8-1112.

[14] K. Abe, S. Iwamoto, H. Yano, Obtaining cellulose nanofibers with a uniform width of 15 nm from wood, Biomacromolecules 8(10) (2007) 3276-3278.

[15] S. Iwamoto, A.N. Nakagaito, H. Yano, Nano-fibrillation of pulp fibers for the processing of transparent nanocomposites, Appl Phys a-Mater 89(2) (2007) 461-466.

[16] S.C. Espinosa, T. Kuhnt, E.J. Foster, C. Weder, Isolation of Thermally Stable Cellulose Nanocrystals by Phosphoric Acid Hydrolysis, Biomacromolecules 14(4) (2013) 1223-1230.

[17] A. Hirai, O. Inui, F. Horii, S. Yamamoto, M. Tsuji, CELL 132-Effects of added electrolytes on the phase separation behavior in aqueous suspensions of bacterial cellulose microfibrils and on the magnetic alignment of the chiral nematic phase, Abstr Pap Am Chem S 235 (2008).

[18] H. Kargarzadeh, I. Ahmad, I. Abdullah, A. Dufresne, S.Y. Zainudin, R.M. Sheltami, Effects of hydrolysis conditions on the morphology, crystallinity, and thermal stability of cellulose nanocrystals extracted from kenaf bast fibers, Cellulose 19(3) (2012) 855-866.

[19] P. Lu, Y.L. Hsieh, Preparation of rod-like, network-structured, and spherical cellulose

nanocrystals with excellent thermal and mechanical properties, Abstr Pap Am Chem S 237 (2009).

[20] D. Viet, S. Beck-Candanedo, D.G. Gray, Dispersion of cellulose nanocrystals in polar organic solvents, Cellulose 14(2) (2007) 109-113.

[21] H.Y. Yu, Z.Y. Qin, L. Liu, X.G. Yang, Y. Zhou, J.M. Yao, Comparison of the reinforcing effects for cellulose nanocrystals obtained by sulfuric and hydrochloric acid hydrolysis on the mechanical and thermal properties of bacterial polyester, Compos Sci Technol 87 (2013) 22-28.

[22] D. Bondeson, A. Mathew, K. Oksman, Optimization of the isolation of nanocrystals from microcrystalline cellulose by acid hydrolysis, Cellulose 13(2) (2006) 171-180.

[23] M. George, C. Montemagno, Estimation of the sulfur ester content of cellulose nanocrystals prepared by sulfuric acid hydrolysis: a reproducible and fast infrared method, Wood Sci Technol 51(3) (2017) 535-556.

[24] M.A. Hubbe, O.J. Rojas, L.A. Lucia, M. Sain, Cellulosic Nanocomposites: A Review, Bioresources 3(3) (2008) 929-980.

[25] S. Montanari, M. Rountani, L. Heux, M.R. Vignon, Topochemistry of carboxylated cellulose nanocrystals resulting from TEMPO-mediated oxidation, Macromolecules 38(5) (2005) 1665-1671.

[26] P. Shahbazi, T. Behzad, P. Heidarian, Isolation of cellulose nanofibers from poplar wood and wheat straw: optimization of bleaching step parameters in a chemo-mechanical process by experimental design, Wood Sci Technol 51(5) (2017) 1173-1187.

[27] B. Wang, M. Sain, Isolation of nanofibers from soybean source and their reinforcing capability on synthetic polymers, Compos Sci Technol 67(11-12) (2007) 2521-2527.

[28] M. Henriksson, G. Henriksson, L.A. Berglund, T. Lindstrom, An environmentally friendly method for enzyme-assisted preparation of microfibrillated cellulose (MFC) nanofibers, Eur Polym J 43(8) (2007) 3434-3441.

[29] V. Favier, H. Chanzy, J.Y. Cavaille, Polymer Nanocomposites Reinforced by Cellulose Whiskers, Macromolecules 28(18) (1995) 6365-6367.

[30] R.J. Moon, A. Martini, J. Nairn, J. Simonsen, J. Youngblood, Cellulose nanomaterials review: structure, properties and nanocomposites, Chem Soc Rev 40(7) (2011) 3941-3994.

[31] S. Iwamoto, W.H. Kai, A. Isogai, T. Iwata, Elastic Modulus of Single Cellulose Microfibrils from Tunicate Measured by Atomic Force Microscopy, Biomacromolecules 10(9) (2009) 2571-2576.

[32] A. Sturcova, G.R. Davies, S.J. Eichhorn, Elastic modulus and stress-transfer properties of tunicate cellulose whiskers, Biomacromolecules 6(2) (2005) 1055-1061.

[33] M.M. Tang, R. Bacon, Carbonization of Cellulose Fibers .1. Low Temperature Pyrolysis, Carbon 1(3) (1964) 390-390.

[34] R. Bacon, M.M. Tang, Carbonization of Cellulose Fibers .2. Physical Property Study, Carbon 1(3) (1964) 390-390.

[35] P.H. Brunner, P.V. Roberts, The Significance of Heating Rate on Char Yield and Char Properties in the Pyrolysis of Cellulose, Carbon 18(3) (1980) 217-224.

[36] K. Yoshino, R. Matsuoka, K. Nogami, S. Yamanaka, K. Watanabe, M. Takahashi, M. Honma, Graphite Film Prepared by Pyrolysis of Bacterial Cellulose, J Appl Phys 68(4) (1990) 1720-1725.

[37] F.J. Norton, G.D. Love, A.J. Mackinnon, P.J. Hall, Mechanisms of Char Production from Oxidized Cellulose, J Mater Sci 30(3) (1995) 596-600.

[38] H.M. Ng, L.T. Sin, T.T. Tee, S.T. Bee, D. Hui, C.Y. Low, A.R. Rahmat, Extraction of cellulose nanocrystals from plant sources for application as reinforcing agent in polymers, Compos Part B-Eng 75 (2015) 176-200.

[39] X.M. Dong, J.F. Revol, D.G. Gray, Effect of microcrystallite preparation conditions on the formation of colloid crystals of cellulose, Cellulose 5(1) (1998) 19-32.

[40] H.B. Chang, J. Luo, A.A.B. Davijani, A.T. Chien, P.H. Wang, H.C. Liu, S. Kumar, Individually Dispersed Wood-Based Cellulose Nanocrystals, Acs Appl Mater Inter 8(9) (2016) 5768-5771.

[41] V. Favier, G.R. Canova, S.C. Shrivastava, J.Y. Cavaille, Mechanical percolation in cellulose whisker nanocomposites, Polym Eng Sci 37(10) (1997) 1732-1739.

[42] J. George, K.V. Ramana, A.S. Bawa, Siddaramaiah, Bacterial cellulose nanocrystals exhibiting high thermal stability and their polymer nanocomposites, Int J Biol Macromol 48(1) (2011) 50-57.

[43] Y.F. Mo, R. Guo, J.H. Liu, Y. Lan, Y. Zhang, W. Xue, Y.M. Zhang, Preparation and properties of PLGA nanofiber membranes reinforced with cellulose nanocrystals, Colloid Surface B 132 (2015) 177-184.

[44] L.B. Ma, Y. Zhang, Y.J. Meng, P. Anusonti-Inthra, S.Q. Wang, Preparing cellulose nanocrystal/acrylonitrile-butadiene-styrene nanocomposites using the master-batch method, Carbohyd Polym 125 (2015) 352-359.

[45] E. Bahar, N. Ucar, A. Onen, Y.J. Wang, M. Oksuz, O. Ayaz, M. Ucar, A. Demir, Thermal and mechanical properties of polypropylene nanocomposite materials reinforced with cellulose nano whiskers, J Appl Polym Sci 125(4) (2012) 2882-2889.

[46] G.J. Kwon, D.Y. Kim, K.Y. Kang, Effects of low-temperature pretreatment on carbonization of cellulose for the production of biocarbons, J Korean Phys Soc 60(10) (2012) 1814-1817.

[47] H.L. Zhu, F. Shen, W. Luo, S.Z. Zhu, M.H. Zhao, B. Natarajan, J.Q. Dai, L.H. Zhou, X.L. Ji, R.S. Yassar, T. Li, L.B. Hu, Low temperature carbonization of cellulose nanocrystals for high performance carbon anode of sodium-ion batteries, Nano Energy 33 (2017) 37-44.

[48] D.R.D. Souza, J.P. de Mesquita, R.M. Lago, L.D. Caminhas, F.V. Pereira, Cellulose nanocrystals: A versatile precursor for the preparation of different carbon structures and luminescent carbon dots, Ind Crop Prod 93 (2016) 121-128.

[49] L.B. Deng, R.J. Young, I.A. Kinloch, Y.Q. Zhu, S.J. Eichhorn, Carbon nanofibres produced from electrospun cellulose nanofibres, Carbon 58 (2013) 66-75.

[50] H. Darmstadt, C. Roy, S. Kaliaguine, Esca Characterization of Commercial Carbon-Blacks and of Carbon-Blacks from Vacuum Pyrolysis of Used Tires, Carbon 32(8) (1994) 1399-1406.

[51] H. Darmstadt, C. Roy, S. Kaliaguine, Characterization of Pyrolytic Carbon-Blacks from Commercial Tire Pyrolysis Plants, Carbon 33(10) (1995) 1449-1455.

[52] K. Nishimiya, T. Hata, Y. Imamura, S. Ishihara, Analysis of chemical structure of wood charcoal by X-ray photoelectron spectroscopy, J Wood Sci 44(1) (1998) 56-61.

[53] A. Abouelsayed, B. Anis, S. Hassaballa, A.S.G. Khalil, U.M. Rashed, K.A. Eid, E. Al-Ashkar, W. El Hotaby, Preparation, characterization, Raman, and terahertz spectroscopy study on carbon nanotubes, graphene nano-sheets, and onion like carbon materials, Mater Chem Phys 189 (2017) 127-135.

[54] L. Bokobza, J.L. Bruneel, M. Couzi, Raman spectroscopy as a tool for the analysis of carbon-based materials (highly oriented pyrolitic graphite, multilayer graphene and multiwall carbon nanotubes) and of some of their elastomeric composites, Vib Spectrosc 74 (2014) 57-63.

[55] L.G. Cancado, K. Takai, T. Enoki, M. Endo, Y.A. Kim, H. Mizusaki, A. Jorio, L.N. Coelho, R. Magalhaes-Paniago, M.A. Pimenta, General equation for the determination of the crystallite size L-a of nanographite by Raman spectroscopy, Appl Phys Lett 88(16) (2006).

[56] M.S. Dresselhaus, A. Jorio, M.A. Pimenta, Resonance Raman spectroscopy in one-

dimensional carbon materials, An Acad Bras Cienc 78(3) (2006) 423-439.

[57] H.M. Heise, R. Kuckuk, A.K. Ojha, A. Srivastava, V. Srivastava, B.P. Asthana, Characterisation of carbonaceous materials using Raman spectroscopy: a comparison of carbon nanotube filters, single- and multi-walled nanotubes, graphitised porous carbon and graphite, J Raman Spectrosc 40(3) (2009) 344-353.

[58] H.M. Heise, R. Kuckuk, A. Srivastava, B.P. Asthana, Characterization of carbon nanotube filters and other carbonaceous materials by Raman spectroscopy - II: study on dispersion and disorder parameters, J Raman Spectrosc 42(3) (2011) 294-302.

[59] A.M. Keszler, L. Nemes, S.R. Ahmad, X. Fang, Characterisation of carbon nanotube materials by Raman spectroscopy and microscopy - A case study of multiwalled and singlewalled samples, J Optoelectron Adv M 6(4) (2004) 1269-1274.

[60] D.S. Knight, Characterization of Diamonds, Synthetic Diamond Films and Related Carbon Materials by Raman-Spectroscopy, Abstr Pap Am Chem S 202 (1991) 118-Phys.

[61] T.G. Miller, D.B. Fischbach, Structural Characterization of Carbon Materials by Laser Raman-Spectroscopy, Carbon 13(6) (1975) 546-546.

[62] J. Ribeiro-Soares, L.G. Cancado, N.P.S. Falcao, E.H.M. Ferreira, C.A. Achete, A. Jorio, The use of Raman spectroscopy to characterize the carbon materials found in Amazonian anthrosoils, J Raman Spectrosc 44(2) (2013) 283-289.

[63] C. Kim, S.H. Park, J.K. Cho, D.Y. Lee, T.J. Park, W.J. Lee, K.S. Yang, Raman spectroscopic evaluation of polyacrylonitrile-based carbon nanofibers prepared by electrospinning, J Raman Spectrosc 35(11) (2004) 928-933.

[64] J.P. Boudou, Surface chemistry of a viscose-based activated carbon cloth modified by treatment with ammonia and steam, Carbon 41(10) (2003) 1955-1963.

[65] J.P. Boudou, J.I. Paredes, A. Cuesta, A. Martinez-Alonso, J.M.D. Tascon, Oxygen plasma modification of pitch-based isotropic carbon fibres, Carbon 41(1) (2003) 41-56.

[66] A. Cuesta, P. Dhamelincourt, J. Laureyns, A. Martinezalonso, J.M.D. Tascon, Raman Microprobe Studies on Carbon Materials, Carbon 32(8) (1994) 1523-1532.

[67] P. Lespade, A. Marchand, M. Couzi, F. Cruege, Characterization of Carbon Materials with Raman Microspectrometry, Carbon 22(4-5) (1984) 375-385.

[68] M. Nakamizo, R. Kammereck, P.L. Walker, Laser Raman Studies on Carbons, Carbon 12(3) (1974) 259-267.

[69] F. Tuinstra, J.L. Koenig, Raman Spectrum of Graphite, J Chem Phys 53(3) (1970) 1126-&.

[70] F. Tuinstra, J.L. Koenig, Characterization of Graphite Fiber Surfaces with Raman Spectroscopy, J Compos Mater 4 (1970) 492-&.

[71] A. Cuesta, P. Dhamelincourt, J. Laureyns, A. Martinez-Alonso, J.M.D. Tascon, Comparative performance of X-ray diffraction and Raman microprobe techniques for the study of carbon materials, J Mater Chem 8(12) (1998) 2875-2879.

[72] M.S. Dresselhaus, G. Dresselhaus, Intercalation Compounds of Graphite, Adv Phys 30(2) (1981) 139-326.

[73] B. Dippel, H. Jander, J. Heintzenberg, NIR FT Raman spectroscopic study of flame soot, Phys Chem Chem Phys 1(20) (1999) 4707-4712.

[74] T. Jawhari, A. Roig, J. Casado, Raman-Spectroscopic Characterization of Some Commercially Available Carbon-Black Materials, Carbon 33(11) (1995) 1561-1565.

[75] R.S. Ruoff, D.C. Lorents, Mechanical and Thermal-Properties of Carbon Nanotubes, Carbon 33(7) (1995) 925-930.

[76] Z.P. Zhou, X.Y. Dou, L.J. Ci, L. Song, D.F. Liu, Y. Gao, J.X. Wang, L.F. Liu, W.Y. Zhou, S.S. Xie, D.Y. Wan, Temperature dependence of the Raman spectra of individual carbon nanotubes, J Phys Chem B 110(3) (2006) 1206-1209.

[77] H.D. Li, K.T. Yue, Z.L. Lian, Y. Zhan, L.X. Zhou, S.L. Zhang, Z.J. Shi, Z.N. Gu, B.B. Liu, R.S. Yang, H.B. Yang, G.T. Zou, Y. Zhang, S. Iijima, Temperature dependence of the Raman spectra of single-wall carbon nanotubes, Appl Phys Lett 76(15) (2000) 2053-2055.

[78] P.V. Huong, R. Cavagnat, P.M. Ajayan, O. Stephan, Temperature-Dependent Vibrational-Spectra of Carbon Nanotubes, Phys Rev B 51(15) (1995) 10048-10051.

[79] C.L. Angell, I.C. Lewis, Raman-Spectroscopy of Mesophase Pitches, Carbon 16(6) (1978) 431-432.

[80] N.J. Everall, J. Lumsdon, D.J. Christopher, The Effect of Laser-Induced Heating Upon the Vibrational Raman-Spectra of Graphites and Carbon-Fibers, Carbon 29(2) (1991) 133-137.

[81] Z.Q. Li, C.J. Lu, Z.P. Xia, Y. Zhou, Z. Luo, X-ray diffraction patterns of graphite and turbostratic carbon, Carbon 45(8) (2007) 1686-1695.

[82] H. Darmstadt, C. Roy, Surface spectroscopic study of basic sites on carbon blacks, Carbon 41(13) (2003) 2662-2665.

[83] F. Kurosaki, K. Ishimaru, T. Hata, P. Bronsveld, E. Kobayashi, Y. Imamura, Microstructure of wood charcoal prepared by flash heating, Carbon 41(15) (2003) 3057-3062.

[84] O. Paris, C. Zollfrank, G.A. Zickler, Decomposition and carbonisation of wood biopolymers - a microstructural study of softwood pyrolysis, Carbon 43(1) (2005) 53-66.

[85] T. Takahagi, A. Ishitani, Xps Study on the Surface-Structure of Carbon-Fibers Using Chemical Modification and C1s Line-Shape Analysis, Carbon 26(3) (1988) 389-396.

[86] S. Yamauchi, Y. Kurimoto, Raman spectroscopic study on pyrolyzed wood and bark of Japanese cedar: temperature dependence of Raman parameters, J Wood Sci 49(3) (2003) 235-240.

[87] T.S. Chung, J.J. Qin, J. Gu, Effect of shear rate within the spinneret on morphology, separation performance and mechanical properties of ultrafiltration polyethersulfone hollow fiber membranes, Chem Eng Sci 55(6) (2000) 1077-1091.

[88] B.K. Chaturvedia, A.K. Ghosh, V. Ramachandhran, M.K. Trivedi, M.S. Hanra, B.M. Misra, Preparation, characterization and performance of polyethersulfone ultrafiltration membranes, Desalination 133(1) (2001) 31-40.

[89] M. Gholami, S. Nasseri, C.Y. Feng, T. Matsuura, K.C. Khulbe, The effect of heat-treatment on the ultrafiltration performance of polyethersulfone (PES) hollow-fiber membranes, Desalination 155(3) (2003) 293-301.

[90] J.J. Qin, M.H. Oo, H. Lee, Development of polyethersulfone hollow fiber ultrafiltration membrane for removal of NOM., Abstr Pap Am Chem S 225 (2003) U971-U971.

[91] W.F. Yong, T.S. Chung, M. Weber, C. Maletzko, New polyethersulfone (PESU) hollow fiber membranes for CO2 capture, J Membrane Sci 552 (2018) 305-314.

[92] P. Qu, H.W. Tang, Y.A. Gao, L.P. Zhang, S.Q. Wang, Polyethersulfone Composite Membrane Blended with Cellulose Fibrils, Bioresources 5(4) (2010) 2323-2336.

[93] P. Daraei, N. Ghaemi, H.S. Ghari, M. Norouzi, Mitigation of fouling of polyethersul fone membranes using an aqueous suspension of cellulose nanocrystals as a nonsolvent, Cell ulose 23(3) (2016) 2025-2037.

Acknowledgements

It would never have been possible to complete this master's thesis without the help, guidance and support of many people.

First and foremost, I would like to express gratitude and special thanks to my advisor, Professor Han Gi Chae. He offered me a precious chance to join his lab, and it was a great pleasure to be a member of PNC Lab. Without his unbounded confidence, incredible patience and timely wisdom, my work would have been an overwhelming pursuit. His counsel and advice on both research and my career have been priceless. It would also like to show my deep appreciation to Professor Myoung Hoon Song and Hyun-Wook Lee for serving as my committee members despite their busy schedule. They let me have my defense an enjoyable time, and their insightful comments and suggestions improved my thesis quality. Many thanks to our lab members, Dr. Young Ho Eom and Dr. Sang-Ha Hwang for their helpful advice and Jeong Eun Lee, Hye Jin Ju, Kyeong Hun Choi, So Jeong Heo and Yea Eun Kim for their cooperation and commitment. I could spend pleasant time in the lab thanks to them.

I am grateful to my family members, my parents, younger sister and younger brother. They always support and encourage me both materially and spiritually.